Matthew Emes, Azadeh Jafari, Andreas Pfahl, Joe Coventry, Maziar Arjomandi

A review of static and dynamic heliostat wind loads

Solar Energy, 2021; 225:60-82

Final publication at: http://dx.doi.org/10.1016/j.solener.2021.07.014

A review of static and dynamic heliostat wind loads

Matthew J. Emes*[1], Azadeh Jafari[1], Andreas Pfahl[2], Joe Coventry[3], Maziar Arjomandi[1]

[1] Centre for Energy Technology, School of Mechanical Engineering, The University of Adelaide, SA 5005, Australia

[2] German Aerospace Center (DLR), Institute of Solar Research, Professor-Rehm-Str. 1, 52428 Juelich, Germany

[3] School of Engineering, College of Engineering and Computer Science, Australian National University, Canberra ACT 2601, Australia

Abstract

Accurate estimation of the static and dynamic wind loads on heliostats based on detailed measurement and characterisation of turbulence is crucial to avoid structural failure and reduce the cost of the structural heliostat components. Wind load predictions for heliostats are not specified in design standards for buildings because of a heliostat's non-standard shape and the variations of wind velocity and turbulence in the lowest 10 m of the atmospheric boundary layer (ABL). This paper reviews the static and dynamic wind loads on heliostats in the most unfavourable operating and stow positions, with a focus on the aerodynamic effects related to the heliostat structural component geometry, turbulence parameters in the ABL and field spacing. An increased resolution of field-scale wind measurements at heliostat field sites is recommended to fully characterise the ABL turbulence, as the high-intensity gusts over shorter durations at heights below 10 m lead to high-amplitude displacements with larger frequencies than observed in standard building structures. Increased understanding and development of aerodynamic wind load predictions for heliostats, based on their critical scaling parameters and local wind conditions, would increase the accuracy of annual field efficiency models through an improved resolution of operating load data and reduce the capital cost of structural components in power tower plants.

Keywords: heliostat; wind load; aerodynamics; atmospheric boundary layer; turbulence

Nomenclature

A	Surface area of heliostat panel (m^2)
AR	Aspect ratio (width/height) of heliostat panel = b/c
α_U	Exponent of power law velocity profile
α	Elevation angle of heliostat panel (°)

β	Angle of attack of wind with respect to heliostat (°)
b	Width of heliostat panel (m)
c	Chord length of heliostat panel (m)
c_{Fi}	Coefficient of force F_i where $i = x, z$
c_{Mi}	Coefficient of moment M_i where $i = Hy, y, z$
δ	Atmospheric boundary layer depth (m)
δ_{ASL}	Atmospheric surface layer depth (m)
d_f	Foundation pile depth (m)
F_x	Drag force on heliostat (N)
F_z	Lift force on heliostat (N)
f	Frequency (Hz)
G_u	Gust factor of wind velocity
H	Elevation axis height of heliostat (m)
I_u	Turbulence intensity of longitudinal velocity component
I_w	Turbulence intensity of vertical velocity component
k	Von Karman's constant
l_{px}	Distance to the centre of pressure from the heliostat elevation axis (m)
L_u^x	Integral length scale of longitudinal velocity component (m)
L_w^x	Integral length scale of vertical velocity component (m)
M_{Hy}	Hinge moment about elevation axis of heliostat (Nm)
M_y	Overturning moment about base of heliostat pedestal (Nm)
M_z	Azimuth moment about vertical axis of heliostat pedestal (Nm)
ρ	Density of air (kg/m^3)
p	Differential pressure between upper and lower surface (Pa)
r	Displacement (mm)
S_{uu}	Longitudinal velocity spectrum (m^2/s)
S_{ww}	Vertical velocity spectrum (m^2/s)
θ	Mean potential temperature (°C)
U_H	Mean velocity at elevation axis height of heliostat (m/s)
U_∞	Freestream velocity in the ABL (m/s)
u_τ	Friction velocity (m/s)
x	Longitudinal/streamwise direction (m)
y	Lateral/spanwise direction (m)
z	Height (m)
z_0	Logarithmic velocity profile surface roughness height (m)

1. Introduction

The application of concentrating solar thermal (CST) power tower technology is emerging as a means for industrial process heating and dispatchable renewable electricity production. Thermal energy is collected by a receiver located at the top of a central tower where solar radiation is concentrated by a large field of heliostats through two-axis tracking of the sun. Cumulative installed capacity of power tower plants increased by five times to approximately 6.3 GW and their levelised cost of electricity (LCOE) decreased by 47% to USD $0.182/kWh between 2010 and 2019 (IRENA 2020). During this time, the capacity factor of deployed commercial-scale power tower plants increased from 30% to 45% through increased power cycle efficiencies operating at high temperatures (Mehos *et al.* 2017) and increased energy storage capacity from 5 hours to 7.7 hours at sites with larger direct solar resources (IRENA 2020). According to projections by IRENA, the LCOE will further decrease to USD $0.07-0.08/kWh for power tower plants commissioned in 2021. One promising opportunity to achieve a reduction in the LCOE is by reducing the heliostat field cost, which contributes approximately 40-50% of the total plant cost (Kolb *et al.* 2011; Pfahl *et al.* 2017a). Currently the total cost of industrial scale heliostats is estimated as USD $140/m^2 by National Renewable Energy Laboratory (NREL) (Turchi *et al.* 2019), with the 2030 DOE target set at USD $50/m^2 (Department of Energy 2017). The most typical heliostat design in the current commercial CST plants, such as the 50 MW Khi Solar One heliostat field in Figure 1(a), consists of glass mirror facets supported by steel beams and trusses and a T-shaped pedestal and torque tube with azimuth and elevation drives for tracking (Téllez *et al.* 2014). Techno-economic analysis by Emes *et al.* (2020a) found that the steel support structure components (Figure 1b) increased their contribution from 18% to 34% of the total heliostat cost due to increased wind loads with increasing heliostat size from 25 m^2 to 150 m^2. Furthermore, the total heliostat cost was reduced by 40% and the optimal heliostat size increased from 25 m^2 to 50 m^2 by lowering the stow design wind speed from 20 m/s to 10 m/s (Emes *et al.* 2015). To achieve the cost reduction targets, innovative designs of the heliostat structural components must be developed to reduce their manufacturing and installation cost (Pfahl 2014a; Pfahl *et al.* 2017a). This requires a detailed understanding of the flow field aerodynamics for a reliable estimation of the wind loads on heliostats.

(a) (b)

Figure 1. Photographs of (a) the 50 MW Khi Solar One heliostat field (Abengoa Solar 2016), and (b) structural heliostat components of the Abengoa Solar heliostat, adapted from Advisian Worley Group (2021).

Heliostats are exposed to atmospheric wind that imposes unsteady loads on the drives, torque tube, pylon, foundation and mirror trusses. Overestimation of the design wind loads increases the capital cost of a solar plant. The wind-bearing heliostat components are designed for a serviceability condition with stiffness to minimise local deformations of the mirror surface during operation at different elevation angles ($\alpha > 0°$), and a survivability condition with strength against the maximum loads during high-wind events (e.g. gust front, storm) when the heliostat surface is aligned horizontally ($\alpha = 0°$) in the stow position. The aerodynamics of these two conditions vary significantly: operating heliostats are characterised by bluff body features including maximum drag forces with increasing surface area with respect to the approaching wind and vortex shedding from the sharp edges of rectangular heliostat mirrors. Stowed heliostats are characterised by slender streamlined body features including maximum lift forces in a highly turbulent flow generated by upstream roughness in the atmospheric boundary layer (ABL). Furthermore, the dynamic wind loads induced by coupling between the temporal variations of the wind loads and the dynamic properties of the heliostat structure, lead to oscillations of the heliostat surface that impacts the tracking (mirror orientation) accuracy and optical performance of the heliostat field.

Evaluation of the maximum wind loads at the appropriate temporal resolution is essential for the cost-effective design of heliostats, since a wide range of sizes and structural designs is currently deployed in the CST industry. Historically, design wind loads on industrial-scale heliostats incorporated aerodynamic coefficients using scaled models of the heliostats in boundary layer wind tunnel experiments. The non-dimensional aerodynamic coefficients for the drag and lift forces on the heliostat surface, and the bending moments about the elevation axis, vertical axis and base of the pylon, were applied following benchmark wind tunnel studies by Peterka *et al.* on isolated heliostats. Peterka and Derickson (1992) measured the mean and peak wind load coefficients in a simulated ABL with a turbulence intensity $I_u = \sigma_u/\overline{U}_H = 18\%$, denoted as the root-mean-square of the longitudinal velocity component to the mean wind speed at the elevation axis height H of a square-facet heliostat model (c = 0.27 m, $H = 0.13$ m). The forces and moments were calculated using high-frequency base force balance measurements on the heliostat model (Peterka *et al.* 1988; Peterka *et al.* 1989). The maximum aerodynamic load coefficients on a scaled model heliostat (Peterka *et al.* 1988; Peterka *et al.* 1989; Peterka and Derickson 1992) were reported in the simulated ABL representing an open country terrain ($z_0 = 0.03$ m) with $I_u = 18\%$ and $G_u = 1.6$ at the heliostat elevation axis height. It has been widely acknowledged that the aerodynamic coefficients in this benchmark study were reported for a single case, whereas the mean wind speed and turbulence intensity profiles of the ABL approaching the heliostat vary significantly with height and surface roughness. The unsteady pressure distribution on the mirror panel due to turbulence in the wind imposes highly fluctuating moments, which can create maximum loads on the heliostat pedestal, foundation and drives. Assessment of the dynamic response of the heliostats under unsteady wind loads is necessary for preventing structural failure due to resonance and buffeting (Pfahl *et al.* 2017a), which may result from the convergence of the dominant frequency of the wind fluctuations to the natural frequency of heliostat structures in the typical range of 1.6–3 Hz (Griffith *et al.*, 2011; Gong *et al.*, 2012; Vásquez-Arango *et al.*, 2015). Deformations and displacements of the heliostat structural elements caused by unsteady pressure distributions and dynamic amplification of peak wind loads impacts the ability of heliostats to withstand strong wind gusts in the stow position at high wind speeds (Emes *et al.* 2017; Vasquez Arango *et al.* 2017; Emes *et al.* 2018; Pfahl 2018; Jafari *et al.* 2019a). Numerical methods, such as Large Eddy Simulation (LES), are generally associated with large computational effort and uncertainties to model the fluctuating wind loads due to ABL turbulence and the transient response characteristics of heliostat structures. RANS methods would be less extensive but are not suitable to simulate the upstream turbulence structures. Hence, experimental data through wind tunnel and field measurements of the ABL turbulence characteristics are usually obtained in the design of a heliostat field, for the assessment of operational performance models and feasibility analyses of power tower systems.

Heliostats in operating positions act as bluff bodies within the ABL, where the interaction of their wakes with the incoming highly turbulent flow results in the aerodynamics of multiple heliostats varying significantly from a single body. The vortices shed by an upstream heliostat or the tower can create vibrations and unsteady loads, due to the fluctuating turbulence component of wind velocity, on the downstream in-field heliostats positioned in the intermediate wake. Due to a blocking effect caused by upstream heliostats, wind tunnel measurements on an array of heliostats in multiple rows reveal that reducing the distance between heliostats decreases the time-averaged loads on the heliostats in the inner rows (Peterka *et al.* 1986). Peterka *et al.* (1987) In comparison to a heliostat in the first row, the mean drag force and hinge moment coefficients on an instrumented heliostat in the fourth row of a four-row array with low and high field densities were decreased by 10% to 50%. In comparison to a heliostat in the first row, the peak drag force on the heliostat in the fourth row increased by 40% (Peterka *et al.* 1987). Hence, the distance between heliostat rows and the layout of heliostat rows in a field impact the mean and peak wind loads on heliostats differently throughout a field.

This paper presents a review of the literature on the wind loads and aerodynamics of heliostats, with the aim to highlight the key parameters that impact the accuracy of wind load predictions in the design and development of industrial-scale azimuth-elevation heliostats. A solid understanding of the wind loads is a major driver to reduce the structural cost of the heliostat field, without compromising the field efficiency and power tower plant performance. Section 2 discusses the temporal and spatial distributions of turbulence, including the state-of-the-art experimental modelling techniques for simulation of the ABL in a wind tunnel and the similarity requirements for heliostat wind load measurements over the range of surface roughness at different field sites. Section 3 describes the conventional coordinate system of an azimuth-elevation heliostat and discusses the effect of the geometry of a heliostat concentrator and its supporting structure components on the wind loads. Field experiment investigations focusing on the dynamic wind load effects on heliostat vibration and tracking error due to the distribution of surface pressures and wind-induced oscillations are outlined in Section 4, followed by a discussion of the wind loads in a heliostat array representing a section of field and the flow around multiple heliostats in Section 5. The key aspects of the literature that are critical to the development of wind load design guidelines for heliostats and future research opportunities for wind load reduction are discussed in Section 6.

2. Atmospheric boundary layer modelling

The atmospheric boundary layer (ABL) is the lowest 1-2 km of the troposphere, where the mechanical properties of the wind are directly influenced by the Earth's surface (Stull 1988). The lower 100 m of the ABL, where heliostats and other physical structures including buildings and bridges are positioned, is known as the atmospheric surface layer (ASL). Surface friction and vertical temperature gradient are two important parameters that influence the wind structure in the ASL (Kaimal and Finnigan 1994). Turbulence in the ASL during near-neutral stability conditions relevant to heliostat design wind speeds is mechanically generated by shear from the terrain surface roughness, with a negligible impact of the mean potential temperature gradient $\partial\theta/\partial z = 0$ and the net vertical heat flux $\overline{w'\theta'} = 0$ (Stull 2005). The wind velocity profile in a neutral boundary layer is conventionally modelled as a logarithmic profile in wind engineering applications, such as the ultimate design wind loads on heliostats at high wind speeds during storms and gust fronts.

2.1. Effect of surface roughness on wind speed and turbulence profiles

The aerodynamic surface roughness determines the velocity and turbulence characteristics over a terrain, based on the height and surface roughness (Simiu and Scanlan 1996). Wind speed is commonly decomposed into a time-averaged mean component and a fluctuating turbulent component. The mean velocity profile in the ABL has been modelled to various degrees of accuracy by the logarithmic law and power law (Kaimal and Finnigan 1994; Xu 2013), respectively:

$$U(z) = \frac{u_\tau}{k}\ln\left(\frac{z}{z_0}\right), \quad (1)$$

$$U(z) = U_\infty\left(\frac{z}{\delta}\right)^{\alpha_U}, \quad (2)$$

where U_∞ (m/s) is the freestream wind speed, δ (m) is the boundary layer depth, u_τ is the friction velocity, κ is von Karman's constant equal to 0.4, z_0 is the aerodynamic surface roughness height, and

α_U is the power law exponent that characterises the level of surface roughness. The depth δ of the neutrally stratified ABL can vary between a few hundred metres to several kilometres, depending on the surface roughness of the terrain (Xu 2013). Typical values of z_0 for different terrains are shown in Figure 2, varying in scale from millimetres in a very flat terrain (e.g. desert) to metres in an urban terrain. The zero-plane displacement is negligible for small surface roughness lengths, such as flat and open-country terrains (Cook 1985), where heliostats are usually located. With increased surface roughness and at lower heights in the ASL, the gradient of the velocity profile increases. . Hence, more gusty wind conditions occur due to the increasing fluctuating wind speed component due to turbulence close to the surface.

The power law has been shown to be suitable for modelling the mean velocity profile at heights around 30-300 m, and thus it is most widely used for study of wind loads on tall buildings and other large civil structures (Xu 2013). Initially derived from the turbulent boundary layer on a flat plate, the logarithmic law has been demonstrated to be most suitable for modelling the mean velocity profile at heights below 100 m, representing the average depth δ_{ASL} of the atmospheric surface layer (ASL) (Cook 1997; Li *et al.* 2010; Sun *et al.* 2014). The logarithmic law provides an accurate velocity profile independent of atmospheric stability for heights below 10 m very close to the ground (Kaimal and Finnigan 1994), and is therefore appropriate for modelling the mean velocity profile for study of wind loads on heliostats.

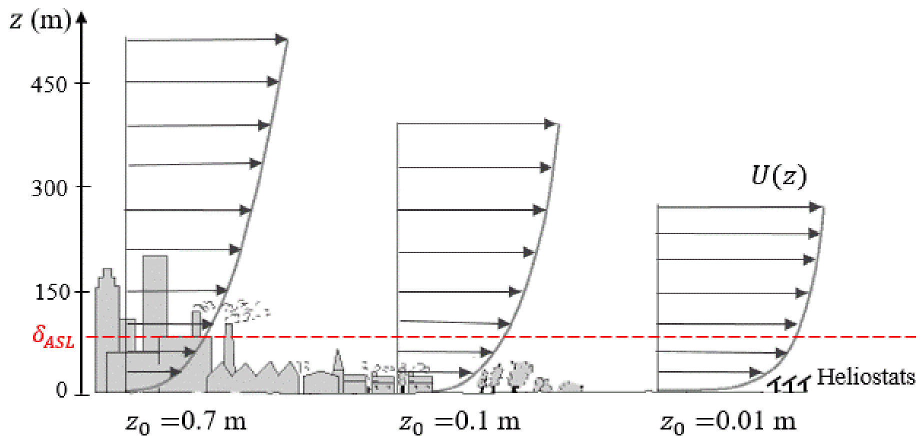

Figure 2. Effect of surface roughness on wind velocity profiles in the atmospheric boundary layer. Adapted from Gilooly and Taylor-Power (2016).

Statistical parameters of turbulence in the ABL are typically used to determine the wind velocity fluctuations. Turbulence intensity is representative of the amplitude of velocity fluctuations compared to the mean velocity, defined as:

$$I_i = \frac{\sigma_i}{U} \ , \tag{3}$$

where σ_i is the standard deviation of the velocity component $i = u, v, w$ in the longitudinal, lateral, and vertical directions, respectively. Turbulence in the lowest 10 m of the ASL is anisotropic and the intensity of the turbulent fluctuations is the largest in the streamwise direction. Figure 3 shows the dependence of the longitudinal (I_u) and vertical (I_w) turbulence intensity on the height z from the ground, and the aerodynamic surface roughness height z_0 defined in the logarithmic velocity profile in equation 1. The profiles of turbulence intensity are genertaed from semi-empirical data in ESDU 85020 (2001) for $U = 20$ m/s at $z = 10$ m, with an estimated uncertainty of ±10% within the full-scale ABL with uniform terrain roughness for an upwind fetch distance of 30 km. The level of surface roughness impacts the magnitude and gradient of I_u, where the intermediate "open country" terrain ($z_0 \approx$ 0.01-0.05 m) is commonly defined in wind engineering study of buildings and heliostats. For instance, in Figure 3(a) at $z = 6$ m that approximates the hinge height of a 120 m^2 heliostat, I_u increases from 0.14 in a very flat terrain ($z_0 = 0.003$ m) to 0.3 in a suburban terrain ($z_0 = 0.3$ m). According to the empirical relationships in ESDU 85020 (2001) derived from atmospheric data, σ_v/σ_u and σ_w/σ_u in the ASL are approximately equal to 0.78 and 0.55 at lower heights where $z \ll \delta$. The average depth δ of the atmospheric boundary layer during neutral stability conditions is typically between 450 m and 600 m, depending on the terrain roughness (Counihan 1975; Xu 2013). Hence, the vertical turbulence intensities in Figure 3(b) follow a similar trend and are approximately half the magnitude of the longitudinal turbulence intensities.

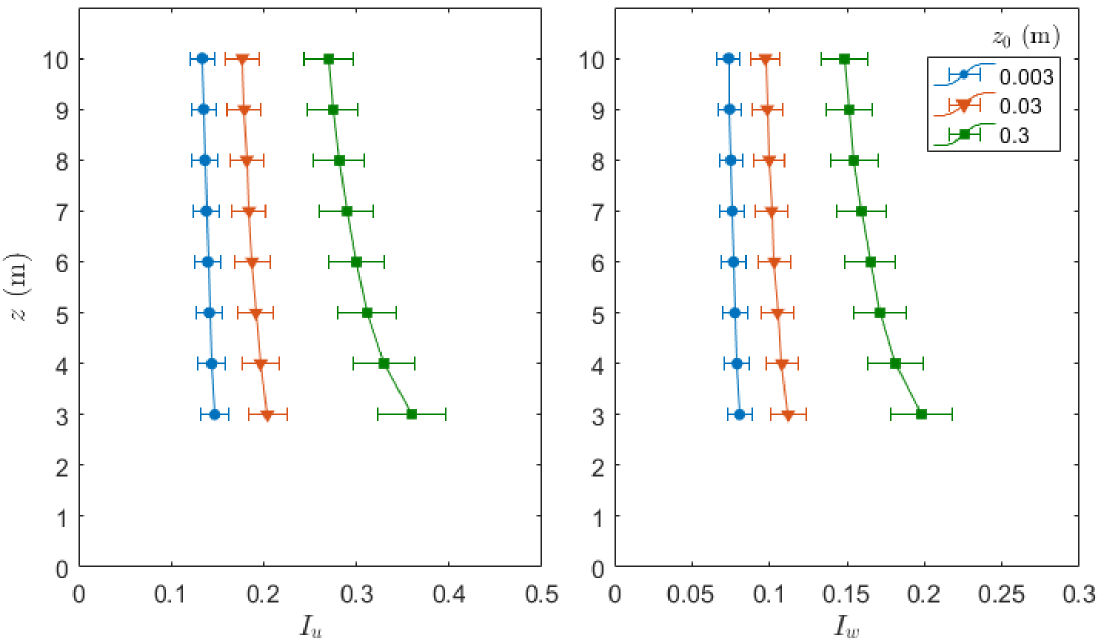

(a) (b)

Figure 3. (a) Longitudinal I_u, and (b) vertical I_w turbulence intensity profiles in the lower 10 m of ABL for different values of surface roughness height z_0 (ESDU 85020 2001). Error bars indicate ±10% uncertainty of turbulence intensity for equilibrium conditions in the neutral ASL with $U = 20$ m/s.

Turbulence in the atmospheric flow is dependent on the features of the terrain and varies based on the site of different heliostat fields. With increasing height from the ground, turbulence intensity decreases in Figure 3 while the integral length scale of turbulence increases in Figure 4 (ESDU 85020 2001). The integral length scale of turbulence represents the average size of the energy-containing eddies within a turbulent boundary layer. Therefore, based on the height of the heliostats from the ground and the terrain surrounding the heliostat field, the turbulence intensities and length scales show a very large variation in the lowest 10 m of the ASL. Commercial-scale heliostats are manufactured with hinge heights in a typical range between 3 m and 6 m. ESDU 85020 (2001) predicts the longitudinal integral length scale L_u^x in Figure 4(a) to range from 27 m to 63 m in an open country terrain ($z_0 = 0.03$ m) and from 50 m to 100 m in a very flat terrain ($z_0 = 0.003$ m) with increasing z from 3 m to 6 m. The average longitudinal extent of the energetic eddies is therefore typically the same order as the chord length of the heliostat and up to an order of magnitude larger. Eddies that are similar in size to the heliostat panel characteristic length are presumably responsible for the peak wind loads on heliostats in stow position, as turbulence length scales that are comparable with the length scale of the structure create a well correlated pressure distribution on the structure (Mendis *et al.* 2007). This is because smaller eddies do not cause high net pressures that are correlated over the heliostat surface, whereas considerably larger eddies have significantly lower vertical velocity fluctuations at the elevation axis height of the heliostat (Pfahl *et al.* 2015). Furthermore, the vertical component of the fluctuating velocity, defined by the vertical integral length scales L_w^x in Figure 4(b), increases from 2.2 m to 5.3 m in an open country terrain ($z_0 = 0.03$ m) and from 4.1 m to 8.3 m in a very flat terrain ($z_0 = 0.003$ m) with increasing hinge height from 3 m to 6 m. The integral length scales of the vertical velocity component are similar in magnitude to the heliostat chord length, which impacts the surface pressure distribution and the maximum hinge moment on a heliostat in stow position. The interaction of the energetic eddies with similar sizes to the heliostat (i.e. $L_w^x/c \approx 1$) are therefore speculated to be responsible for dynamic effects observed in the field, such as aeroelastic flutter and fatigue loads on heliostats.

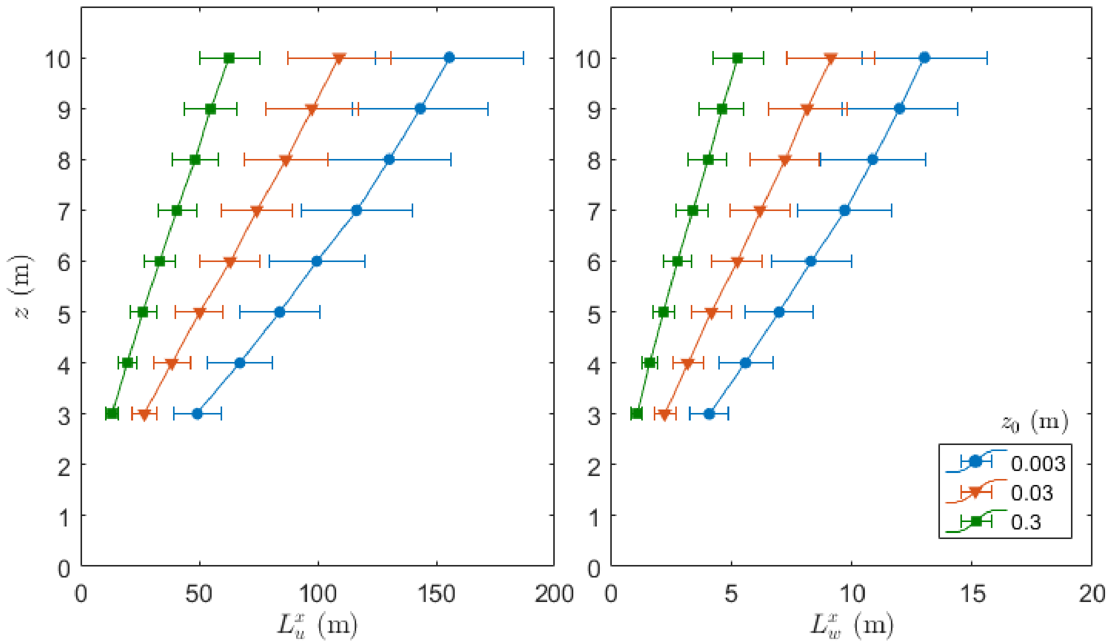

(a) (b)

Figure 4. (a) Longitudinal and (b) vertical integral length scales of turbulence as a function of height z and surface roughness height z_0 (ESDU 85020 2001). Error bars indicate ±20% uncertainty of integral length scales for equilibrium conditions in the neutral ASL with $U = 20$ m/s.

2.2. Scaling of heliostat models and turbulence spectra

The mismatch of scaling ratios, between the ABL thickness and chord length of the heliostat, is an important consideration in wind tunnel modelling of heliostats due to their small dimensions compared to the ABL. It is possible to model heliostats with the same scaling ratio as the ABL, due to the due to technological constraints in modelling the structural details and measurement of the pressure and forces on a heliostat model. Therefore, heliostats are usually modelled using higher scaling ratios. between 1:10 to 1:50. This results in violated similarity of the Reynolds number and the turbulence spectra between wind tunnel experiments and the full-scale condition. The impact of Reynolds number similarity can be overcome on sharp-edged models at Reynolds numbers above 50,000 (Tieleman 2003). This has been demonstrated by the independence of aerodynamic coefficients of heliostats with Reynolds number at freestream velocities between 5 m/s and 35 m/s (Pfahl and Uhlemann 2011b). However, the turbulence fluctuations and their spectral distribution with the wide range of frequencies in the ABL affect the wind loads significantly (Jafari *et al.* 2019b).

Figure 5 schematically presents the range of dimensions of a model heliostat in three sets of wind tunnel experiments studies (Peterka *et al.* 1989; Pfahl *et al.* 2011a; Emes *et al.* 2017) and compares the geometric scaling of a full-scale heliostat and ABL with their respective models in a wind tunnel. These studies measured wind loads, expressed as aerodynamic coefficients of drag, c_{Fx}, and lift, c_{Fz}, forces, and the moments induced at the hinge, c_{MHy}, the foundation, c_{My} and the vertical azimuth axis, c_{Mz}, as shown in Figure 5(b) on heliostat models in stow position and inclined at different elevation angles (α) in operating positions:

$$c_{Fx} = \frac{F_x}{1/2\rho U_H^2 A}, \tag{4}$$

$$c_{Fz} = \frac{F_z}{1/2\rho U_H^2 A}, \tag{5}$$

$$c_{MHy} = \frac{M_{Hy}}{1/2\rho U_H^2 Ac}, \tag{6}$$

$$c_{My} = \frac{M_y}{1/2\rho U_H^2 AH}, \tag{7}$$

$$c_{Mz} = \frac{M_z}{1/2\rho U_H^2 Ac}, \tag{8}$$

where c is the heliostat chord length in the longitudinal (windward) direction, H is the elevation axis (hinge) height, and U_H is the time-averaged wind speed at the height of heliostat elevation axis.

Standard practice in scale-model simulations determines the geometric scaling ratio of a heliostat model considering the effects of both terrain and height, and the spectrum of the simulated boundary layer in a wind tunnel (Cook 1978). Heliostat models were positioned in a simulated boundary layer with the mean velocity profile and turbulence intensity matched to the ABL in an open-country terrain in wind tunnel tests. Peterka *et al.* (1989) tested a heliostat model at a scale of 1:40 in the Meteorological Wind Tunnel of the Fluid Dynamics and Diffusion Laboratory at Colorado State University. The boundary layer thickness in their wind tunnel simulation was about 1 m, which compared to the average ABL thickness in open terrains suggests a scaling factor of 1:350 for the ABL. The same scaling challenge was evident for the German Aerospace Center (DLR) experiments by Pfahl *et al.* (2011a), where the heliostat model was at a 1:20 scale. A similar heliostat model scaling ratio, which was considerably larger than the ABL scaling ratio of approximately 1:100, was used in the University of Adelaide large-scale wind tunnel by Emes *et al.* (2019a). The difference in scaling ratios is speculated to have led to variations in the reported wind load coefficients for the maximum operational and stow heliostat configurations at different elevation angles (α) with respect to the horizontal in Table 1. This raises uncertainty of the accuracy of the wind load measurements. The similarity of wind tunnel experiment simulations for the evaluation of heliostat wind loads can be verified by an instrumented full-scale heliostat prototype at a field site, however such data has been scarcely reported in the literature (Jafari *et al.* 2019b).

Table 1. Comparison of peak operational and stow wind load coefficients reported in the literature.

Wind tunnel experiment	Operation				Stow α=0°				I_u (%)
	α=90°	α=30°	α=90°	α=30°					
	c_{Fx}	c_{Fx}	c_{My}	c_{MHy}	c_{Fx}	c_{Fz}	c_{My}	c_{MHy}	
Peterka *et al.* (1989)	4	2.8	4.35	0.6	0.9	0.6	1	0.2	18
Pfahl *et al.* (2011a), Pfahl *et al.* (2015)	3.3	2.1	3.2	0.55	0.43	0.38	0.53	0.18	18
Emes *et al.* (2019a)	2.25	1.89	2.29	0.21	0.39	0.49	0.43	0.13	13

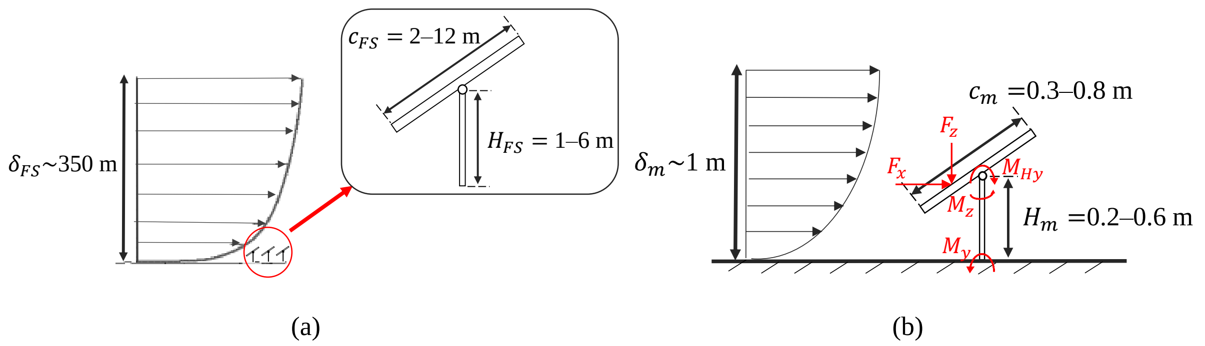

Figure 5. A schematic showing the dimensions of: (a) a full-scale heliostat placed in ABL, (b) a model heliostat in a wind tunnel boundary layer, and the forces and moments on the heliostat model. The dimensions of the

model heliostat are based on the studies in the literature (Peterka *et al.* 1989; Pfahl *et al.* 2011a; Emes *et al.* 2017). The boundary layer thickness is δ, c defines the chord length of the heliostat mirror panel and H is the heliostat hinge height. The subscripts FS and m represent full scale and model scale, respectively.

The power spectral density function of the wind speed provides critical information about the scales of energy-containing turbulent eddies, which is necessary for evaluation of unsteady wind loads on structures. The non-dimensional power spectral density of the velocity fluctuations compares the distribution of turbulence energy in the wind tunnel boundary layer with that predicted by ESDU 85020 (2001) in the ASL through a modified form of the von Kármán (1948) model:

$$\frac{fS_{uu}}{\sigma_u^2} = \frac{4n_u}{(1 + 70.8n_u^2)^{5/6}} \tag{1}$$

$$\frac{fS_{ww}}{\sigma_w^2} = \frac{n_w(1 + 755.2\, n_w^2)}{(1 + 283.2\, n_w^2)^{11/6}} \tag{2}$$

where S_{uu} and S_{ww} are the power spectral density functions of the fluctuating streamwise and vertical velocity components, respectively, and σ_u^2 and σ_w^2 are the streamwise and vertical velocity variances. The non-dimensional frequency is defined as $n_i = fL_i^x/U$, where L_u^x and L_w^x are the integral length scales of the longitudinal and vertical velocity components, respectively. These represent the average size of eddies corresponding to the peak of the turbulence spectrum, which can be determined semi-empirically from the peak spectral frequency, or from the auto-correlation of the fluctuating velocity component (Farell and Iyengar 1999).

Figure 6(a) shows a noticeable shift of the longitudinal power spectra to higher energy levelswith increasing turbulence intensity at a height of 0.3 m within two different wind tunnel boundary layers (Jafari *et al.* 2019a). The shift in the spectral peak to smaller length scales by matching the turbulence intensity also indicates that the low-frequency part of the spectra cannot be reproduced, as due to the wind tunnel's restricted cross-section and length, the generation of turbulent eddies is limited. (Peterka *et al.* 1998; Iyengar and Farell 2001; Banks 2011; Kozmar 2012; De Paepe *et al.* 2016; Leitch *et al.* 2016). A similar trend is shown for the vertical turbulence spectra in Figure 6(b), with a shift to higher frequencies. Pfahl *et al.* (2015) suggested that reproducing the vertical power spectrum is important for evaluating the peak wind loads on a stowed heliostat, because of the linear relationship found by Rasmussen *et al.* (2010) between the vertical spectra and the lift forces and hinge moments on a horizontal flat plate exposed to small vertical turbulence $I_w \leq 10\%$. Jafari *et al.* (2019b) found that turbulent length scales of the same order as the heliostat's chord (windward) length and an order of magnitude larger, corresponding to a range of reduced frequencies, $0.1 < fc/U < 1$, effectively contribute to the unsteady wind loads. Hence, it was proposed by Jafari *et al.* (2019b) that this range of reduced frequencies of the turbulence spectra should be carefully simulated in wind tunnel studies in order to reduce the scaling impact on the measured peak wind loads and provide accurate wind load predictions on the full-scale structure.

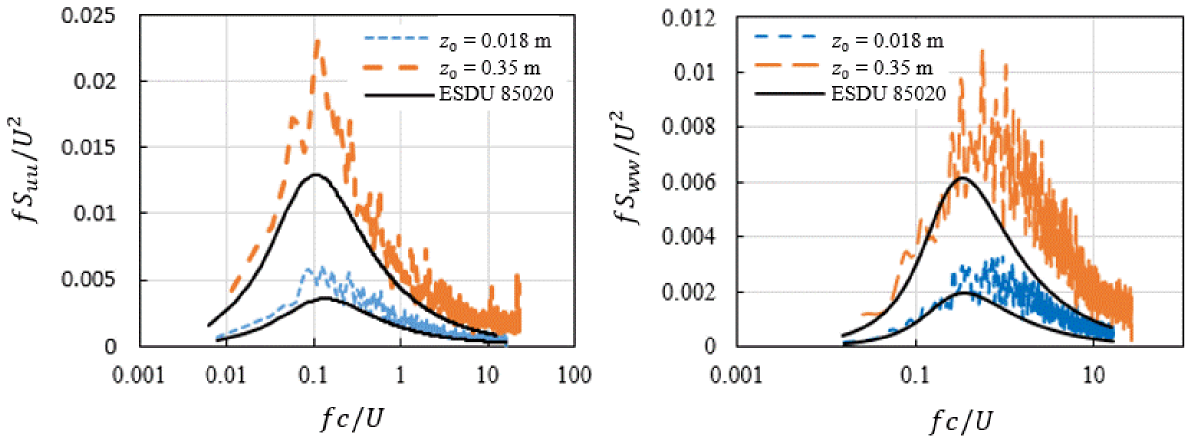

(a) (b)

Figure 6. Comparison of wind tunnel measurements in two simulated ABLs (Jafari *et al.* 2019a) with the modified von Karman form (ESDU 85020 2001) of non-dimensional turbulence spectra of the (a) longitudinal fluctuating component of wind speed u, (b) vertical fluctuating component of wind speed w. Simultaneous matching of both the longitudinal and vertical spectra in the critical range of reduced frequencies cannot be achieved in scaled model wind tunnel experiments. Similarity of turbulence spectra should be applied to the velocity component that contributes to the unsteady wind loads on the heliostat configuration being investigated.

The discrepancies between wind tunnel and atmospheric turbulence spectra bring into question the reliability of wind load measurements and whether they correspond to the wind loads on full-scale heliostats. However, the formation of turbulent eddies in a wind tunnel is restricted by the tunnel's limiting dimensions, therefore the integral length scales in the full-scale ABL cannot be replicated (Jafari *et al.* 2019a). The integral length scales of the vertical velocity component increase with height from the ground in wind tunnel and full-scale measurements. In contrast, the longitudinal length scales are larger near the surface in a wind tunnel boundary layer, where an increased base width of the spires generates large vortices through separation. Regardless of the different mechanisms that create turbulence in the wind tunnel and the lowest 20 m of the full-scale ABL, the increase in L_u^x and the decrease in L_w^x is also seen in the ASL's lower regions due to blocking of the vertical velocity component near the ground (Jafari *et al.* 2019a). Pfahl (2018) concluded that matching the vertical turbulence intensity with full-scale standard data, despite a shift of the streamwise turbulence spectrum to higher frequencies in wind tunnel experiments, was appropriate for determining the lift force and hinge moment measurements on a model-scale stowed heliostat. Hence, the geometric scaling ratio of a heliostat model should be determined according to the turbulence spectrum for the corresponding full-scale structure, considering the effects of both terrain and height, and the spectrum of the simulated boundary layer in a wind tunnel. The geometric scaling ratios for modelling a prototype heliostat in an open-country terrain were determined as an example by Jafari *et al.* (2019b). It was found that similarity of the streamwise velocity spectrum is required to model the unsteady drag force on a vertical heliostat at $\alpha = 90°$ and a 1:20 scale model with larger dimensions showed the closest match to the modified von Karman spectrum (ESDU 85020 2001). In contrast, accurate measurement of the unsteady lift force on a stowed heliostat requires similarity of the vertical turbulence spectrum, which showed the closest match to the von Karman spectrum (ESDU 85020 2001) for a 1:60 model with smaller dimensions. The relative contribution of the longitudinal and vertical components of turbulence, for a stowed heliostat and over the range of heliostat operating conditions, should be further verified through wind tunnel and full-scale measurements. Since the unsteady longitudinal and vertical turbulence components are not generated independently using spires and roughness elements, this would require investigation of active methods of turbulence generation. Analysis of wind loads on full-scale heliostats with respect to the incoming wind turbulence measured simultaneously can also verify the scaling effects observed in wind tunnel experiments to provide a more reliable estimation of wind loads.

2.3. Effect of turbulence intensity and length scales on peak wind loads

The impact of turbulence on heliostat wind loads has been widely investigated through systematic wind tunnel experiments in the literature. Further to the variation of the time-averaged component of the wind speed with height and surface roughness in the ABL for the determination of design wind speeds on heliostats, the temporal characteristics are defined by the intensity of the velocity fluctuations and the spatial variations are characterised by the integral length scale of turbulent eddies. Turbulence intensity in the approaching flow is a commonly reported parameter that affects the wind loads on operating and stowed heliostats. Peterka *et al.* (1989) studied the mean and peak wind loads on a heliostat at different elevation angles in simulated boundary layers at I_u =14% and I_u =18%. It was found that with increasing I_u, the peak lift and drag force coefficients increased for all elevation angles, α, of the heliostat panel with respect to the horizontal, with best-fit curves shown by the dashed lines in Figure 7. The maximum drag force coefficient at α = 90° increased from 3 to 4, and the peak lift force coefficient at α = 30° increased from 1.7 to 2.7 by increasing I_u at the heliostat hinge height from 14% to 18%. Furthermore, according to Peterka *et al.* (1987), the peak lift force coefficient on a heliostat at stow increased from 0.5 to 0.9 when I_u increased from 14% to 18%. Peterka *et al.* (1989) discussed that the reason for the increase in the wind loads was not found in their experiments but it was likely to be was linked to the interaction of turbulence and separated shear layers near the plate's edge.

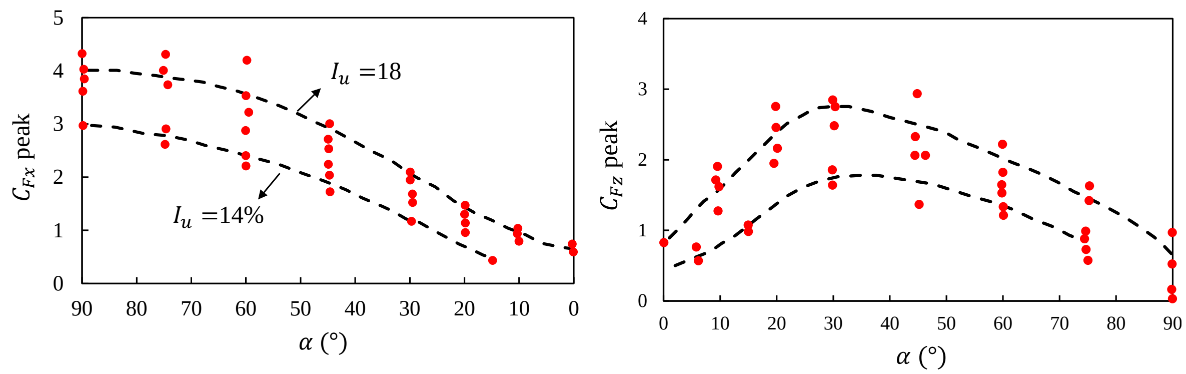

(a) (b)

Figure 7. (a) Peak drag force and (b) lift force coefficients on a heliostat at different elevation angles, α, at I_u=14% and I_u=18%. Reproduced from Peterka *et al.* (1989).

Emes *et al.* (2019a) further investigated the effect of turbulence intensity on the peak aerodynamic hinge and overturning moment coefficients on a single heliostat model, through an extension of turbulent ABLs simulated in previous wind tunnel experiment studies by Peterka *et al.* (1989) and Pfahl *et al.* (2015). The percentages in the legend of Figure 8 indicate the longitudinal turbulence intensity at the hinge height of the heliostat model for open terrains of a range of roughness heights. Increased intensity of turbulence of the approaching ABL flow directly correlated to increases in the peak moment coefficients. The quasi-steady peak values of the force and moment coefficients are determined as the sum of the mean and three-times the standard deviation of the fluctuating moment, with a 99.7% probability of not being exceeded following a Gaussian distribution (Simiu and Scanlan 1996). As reported by Peterka and Derickson (1992), there is an approximately linear increase of the peak coefficients with increasing turbulence intensity at $I_u \geq 10\%$. The difference between the scaling factors of the model-scale ABL and heliostat in wind tunnel experiments with respect to their full-scale counterparts led to variations in the peak wind load coefficients. The relative sizes of the heliostat chord length and the energy-containing eddies is another important factor influencing the range of frequencies that contribute to the generation of fluctuating loads.

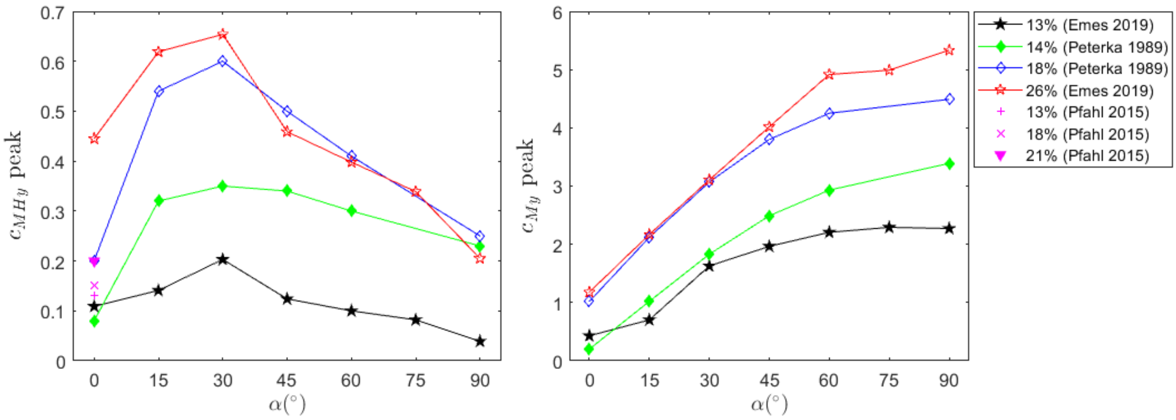

Figure 8. Effect of turbulence intensity I_u (%) and elevation angle α of a heliostat in wind tunnel experiments (Peterka *et al.* 1989; Pfahl *et al.* 2015; Emes *et al.* 2019a) on: (a) peak hinge moment coefficient, and (b) peak overturning moment coefficient.

Due to the anisotropic nature of atmospheric turbulence and depending on the orientation of the heliostat panel, both streamwise and vertical turbulence parameters can be of significance for the wind loads. While in the previous experiments by Peterka *et al.* (1989) and Emes *et al.* (2017), all components of turbulence intensity varied during the experiments, the observed effects on the wind load coefficients were only correlated with longitudinal turbulence intensity and the variations of vertical turbulence components were not differentiated. Pfahl (2018) proposed that at stow position, vertical velocity is more decisive for the pressure forces on the panel as it acts normal to it and therefore the lift force coefficient on a stowed heliostat was suggested to be more closely correlated with vertical turbulence intensity, I_w. The lift force on a stowed heliostat model in a simulated boundary layer was measured in a series of tests, where I_u and I_w varied in the wake of cylinders of different diameters. Figure 9 shows the peak and root mean square (RMS) lift force coefficients as a function of I_u and I_w. Pfahl (2018) discussed that the curve-fitted coefficients showed a better match as a function of I_w, and therefore, I_w

has a stronger effect on the lift force than I_u. This conclusion was drawn from comparison of the lift force coefficients for two cases in the cylinder wake with a heliostat model in a simulated boundary layer with $I_w = 10\%$ was identical. However, the turbulence in the wake of a cylinder is dominated by quasi-static vortex shedding with different vertical turbulence profiles and spectral properties than in the ABL. Pfahl (2018) suggested that the lift force and hinge moment coefficients in stow position were largely dependent on the vertical turbulence intensity compared with dissimilarities of the turbulence spectra. Despite changes in the shape of the spectra affecting the pressure distribution, it was found that the differences in strength and width of the high-pressure suction region near the heliostat mirror panel's edge compensate each other regarding these wind load coefficients.

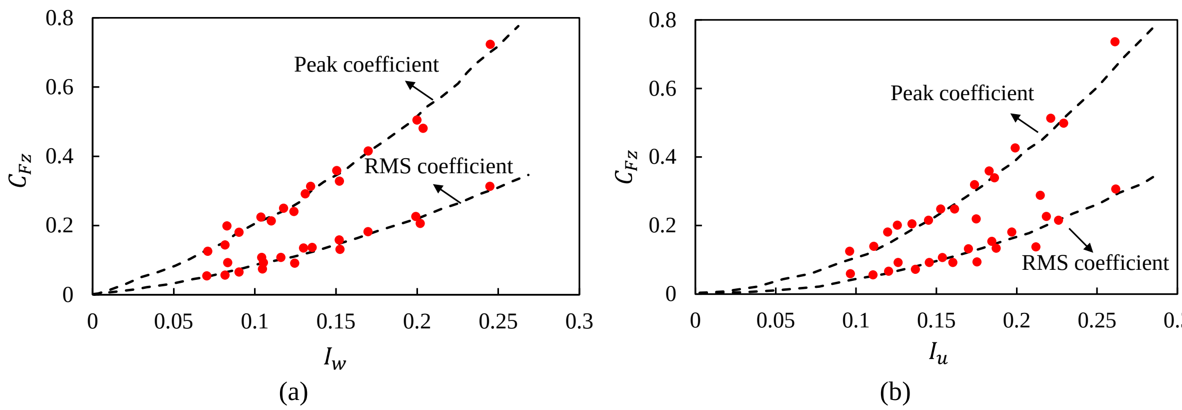

Figure 9. Effect of turbulence intensity on peak and RMS lift force coefficients on a stowed heliostat for: (a) longitudinal turbulence intensity, I_u, (b) vertical turbulence intensity, I_w. Reproduced from Pfahl (2018).

Another important parameter which influences the wind loads is the integral length scale of turbulence in the boundary layer. The ratio of the integral length scale to the heliostat chord length was found to impact the wind loads on a heliostat at stow position. Emes *et al.* (2017) studied the effect of changes in L_u^x/c by measuring the lift force on stowed heliostat models of different chord length dimensions in a modelled atmospheric boundary layer. They found that the peak lift force coefficient increased with increasing L_u^x/c, however both L_u^x/c and L_w^x/c varied simultaneously by changing the chord length dimensions of the heliostat. By stowing a fixed heliostat size with constant c at different heights in a simulated ABL, Jafari *et al.* (2019a) showed that the peak lift coefficient was more strongly correlated with L_w^x/c than L_u^x/c. As shown in Figure 10, the peak lift coefficient increased by 65% when L_w^x/c increased from 0.3 to 0.5 at a constant $L_u^x/c = 1$. In comparison, only a 10% reduction in the lift coefficient was observed with increasing L_u^x/c from 1 to 1.15 at a constant L_w^x/c = 0.5. Hence, this demonstrates that the vertical component of the fluctuating velocity makes a larger contribution to the generation of the lift force on a stowed heliostat. The relative influence of the longitudinal and vertical turbulence components on the heliostat wind loads at intermediate elevation angles, such as the maximum operating lift force and hinge moment at $\alpha = 30°$, should be considered in future investigations.

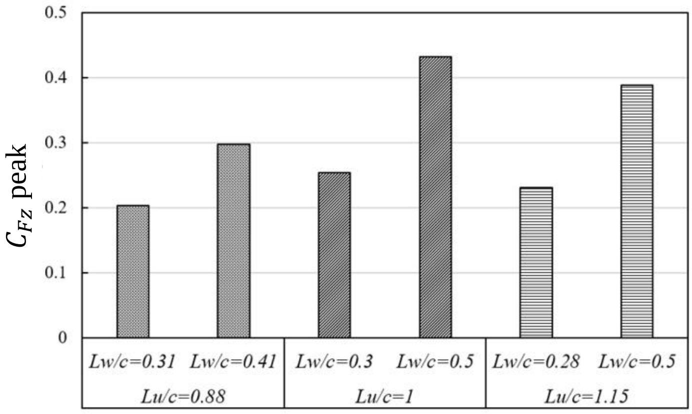

Figure 10. Comparison of peak lift force coefficients in stow position for similar values of L_u^x/c and different values of L_w^x/c in the ABL with $z_0 = 0.018$ m (Jafari *et al.* 2019a).

The combined effects of intensity and integral length scales of turbulence on the aerodynamic load coefficients were studied by measurement of the unsteady wind loads on vertical (α = 90°) and stowed (α = 0°) heliostats in two simulated ABLs by Jafari *et al.* (2018) and Jafari *et al.* (2019a), respectively. Heliostat models of different chord length dimensions between 0.3 m and 0.8 m at a fixed height $H =$ 0.5 m were tested for the maximum drag case on the vertical heliostat. Three chord length dimensions (c = 0.5, 0.6, 0.7 m) with H/c ratios between 0.2 and 1.3 were tested for the maximum lift case on the stowed heliostat. The peak drag force coefficient on a vertical heliostat (Figure 11a) followed a logarithmic function of the longitudinal turbulence intensity and longitudinal integral length scale:

$$c_{Fx} = 1.05 \ln\left[I_u \left(\frac{L_u^x}{c}\right)^{0.48}\right] + 4 \tag{9}$$

In contrast, the peak lift force on a heliostat at stow position (Figure 11b) was shown to correlate with a logarithmic function of the vertical turbulence intensity and length scale:

$$c_{Fz} = 0.267 \ln\left[I_w \left(\frac{L_w^x}{c}\right)^{2.4}\right] + 1.566 \tag{10}$$

The turbulence parameters in equations 9-10 describe the spatial and temporal release of turbulence energy and their effect on the fluctuating load coefficients. The larger exponent of 2.4 in the logarithmic function in equation 10 shows a larger sensitivity of the peak lift force coefficient to L_w^x/c than to I_w. As a result, the influence of the vertical velocity turbulent energy's spatial distribution on the lift force on a stowed heliostat is greater than the vertical velocity turbulent energy's temporal release. In contrast, the smaller exponent of 0.48 indicates that the spatial release of longitudinal energy in the investigated range of L_u^x/c between 1 and 4, has a relatively smaller effect on the peak drag force coefficient on a vertical heliostat. Hence, the peak wind loads on heliostats in the ABL can effectively be estimated for these two critical load cases using the defined turbulence parameter, in terms of the expected full-scale turbulence intensity and length scales that are a function of the surface roughness of the terrain in Figure 3 and Figure 4, respectively.

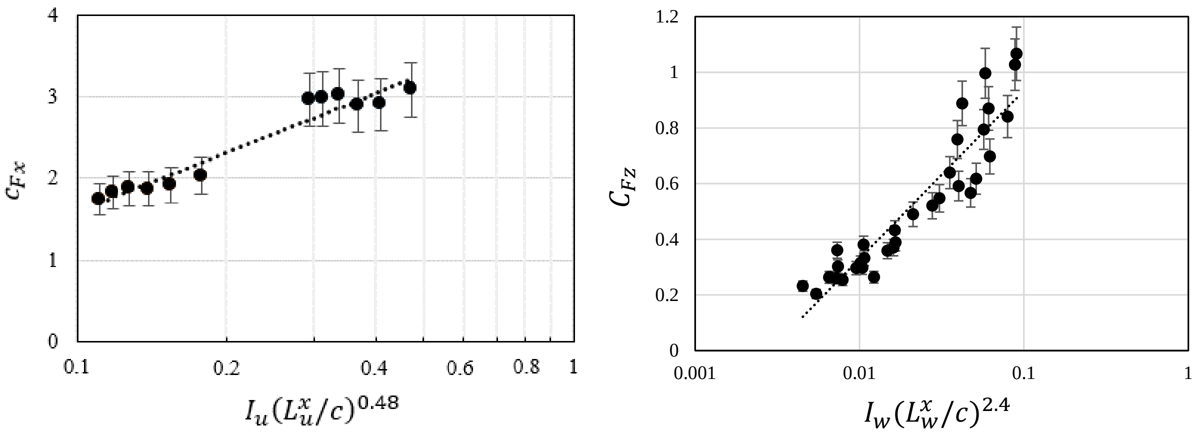

(a) (b)

Figure 11. Peak wind load coefficients on a heliostat: (a) drag force coefficient at α = 90° as a function of longitudinal turbulence intensity and integral length scale (Jafari *et al.* 2018); (b) lift force coefficient at $\alpha = 0°$ as a function of vertical turbulence intensity and integral length scale (Jafari *et al.* 2019a). The dashed lines indicate the logarithmic relationships in equations 9-10 based on the longitudinal and vertical turbulence parameters, respectively.

3. Heliostat geometry effects on wind loads

The wind effects on heliostats are well represented by the bluff body aerodynamics of the large reflecting surface inclined at different elevation and azimuth angles during operation of a power tower plant. Figure 12 shows the wind loads on a conventional azimuth-elevation heliostat, consisting of an array of rectangular glass facets mounted on tubular steel components in a T-shaped configuration to withstand the maximum bending moments about the hinge and the base of the heliostat pedestal. When inclined at different elevation angles, the gap between the lower edge of the heliostat panel and the ground which enlarges as α decreases. The critical scaling parameters that have been investigated in the literature include the aspect ratio of the rectangular heliostat panel in section 3.1, the gaps between the heliostat facets in section 3.2, and the vertical distance between the elevation axis and the ground by the pylon height in section 3.3.

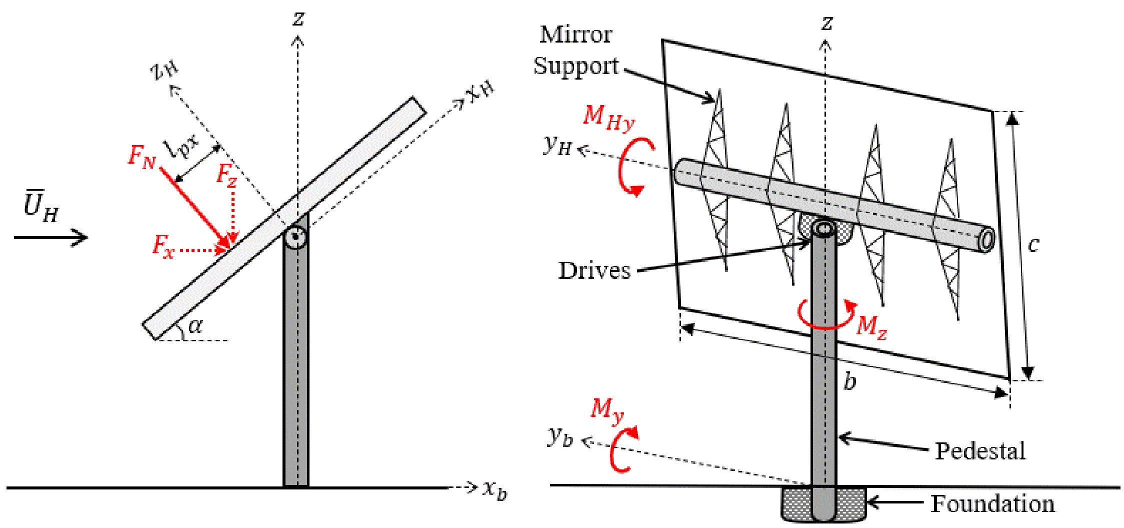

(a) (b)

Figure 12. Schematic diagram of the (a) drag and lift forces on the heliostat surface inclined at elevation angle α, (b) hinge, overturning and azimuth moments on the heliostat components (Emes *et al.* 2020a).

3.1. Aspect ratio

The aspect ratio of the heliostat, defined as the ratio of the width to the height $AR = b/c$ of the panel in Figure 12(b), has a significant but varying impact on the wind load components on a heliostat. The main components of the heliostat that are exposed to wind effects are the foundation, the pedestal, the panel and the elevation and azimuth drives. Figure 13 shows the impact of the aspect ratio of a heliostat panel on the normalised load coefficients for the maximum operating load cases and in stow position ($\alpha = 0°$), based on fitted exponential functions of scale-model heliostat measurements in a boundary layer wind tunnel (Pfahl *et al.* 2011a). It can be observed that M_y about the base of the upright heliostat at $\alpha = 90°$ decreases by approximately 30% at AR = 1.5 and by as much as 60% at AR = 3 relative to a square-shaped heliostat (AR = 1). A reduction in M_y and M_{Hy} with increasing aspect ratio indicates smaller loads on the elevation drive and that the foundation pile depth and pylon diameter can be reduced. However, the M_z on operating heliostat and F_z on stowed heliostat increase by 47% and 30%, respectively, with increasing AR from 1 to 3. Hence, there is a trade-off between the dimensions of the pedestal with the elevation drive and the torque tube with the azimuth drive in the heliostat design.

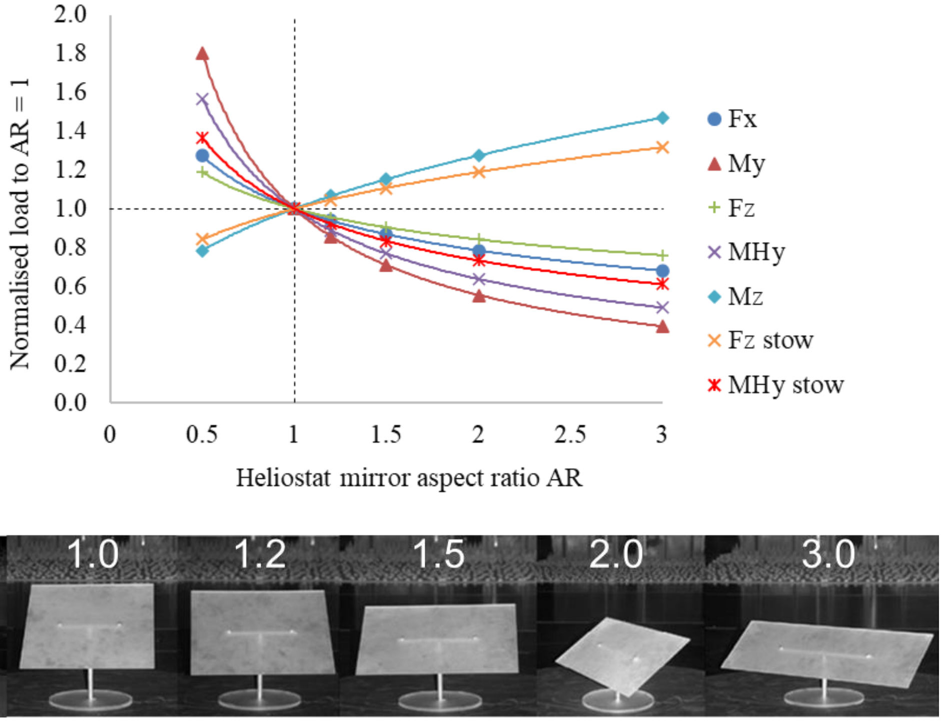

Figure 13. Effect of aspect ratio on the normalised heliostat loads for the maximum wind load configurations during operation and stow. Reproduced from the best-fit power law exponents in Table 3 of Pfahl *et al.* (2011a).

3.2. Facet gap

Conventional heliostats are designed with small gaps between the mirror facets. Wu *et al.* (2010) found that small gaps have a negligible impact on the force and moment coefficients through wind tunnel tests and numerical analysis. However, wider gaps in the mirror panel caused a larger pressure difference at the edges of the gap at the windward corners. This led to a 20% increase of the hinge moment on a heliostat at $\alpha = 30°$, due to a shift of the low-pressure region on the leeward surface away from the central elevation axis for wind flow along the gap at $\beta = 0°$ (Pfahl *et al.* 2011c). The peak hinge moment at stow position with a wide gap was also increased due to a similar effect. Peterka and Derickson (1992) stated that the area represented by slits in the mirror panel can be considered as a solid surface area up to a ratio of 15%. The wind load coefficients were compared with no gap and a heliostat with two mirror facets separated by a wide gap mirror facets. The total mirror area (30 m^2 at full scale, modelling scale 1:20), with a gap width of 0.5 m corresponded to a portion of 8% of the opening. With the exception of the peak operating hinge moment at $\alpha = 30°$ increasing by 20%, there was only a small effect of gap on the wind loads, in agreement with the findings by Peterka and Derickson (1992). The shielding effect of support structure components contributed to small increases in the drag force in stow position and operating load cases with wind impacting the back surface of the heliostat. Hence, the geometry of a heliostat concentrator consisting of facets with narrow gaps can effectively be modelled as a thin flat plate when considering the aerodynamic wind loads on a heliostat, whereas accurate prediction of the dynamic wind loads (refer to Section 4) requires similarity of the structural stiffness and mass distribution of the heliostat support structure.

3.3. Pylon height

Conventional azimuth-elevation heliostats are commonly designed for a ratio of hinge height to mirror chord length, $H/c = 0.5$, increasing to 0.7 for a heliostat with a horizontal primary axis (Téllez *et al.* 2014). As shown in in Figure 14(a), the peak lift coefficient in stow position at $H/c = 0.5$ varies over a range between 0.4 and 0.9, depending on the spectral distribution of ABL turbulence (refer to Section 2.2) and the ratio of the integral length scales to the scale model heliostat characteristic length in different wind tunnel experiments (Emes *et al.* 2017). Measurement of the peak lift force on models with varying pylon heights over a range of H/c between 0.2 and 0.8 was used to study the effect of heliostat hinge height on stow loads. Jafari *et al.* (2019a) found that the lift coefficient on a stowed heliostat followed a linear variation with H/c from 0.5 to 0.2, such as a reduction from 0.3 to 0.2 at $I_w = 9\%$ ($z_0 = 0.018$ m), and from 0.65 to 0.48 at $I_w = 19\%$ ($z_0 = 0.35$ m). The rate of reduction of c_{Fz} with decreasing H/c is larger in the ABL with $z_0 = 0.35$ m, such that the slope of the linear function at $z_0 = 0.35$ m is three times larger than for $z_0 = 0.018$ m. Figure 14(b) shows the peak lift force coefficient on a heliostat at stow, normalised with respect to $H/c = 0.5$ as a function of H/c for different values of aerodynamic roughness length z_0. The peak c_{Fz} on a stowed heliostat within the ABL follows a linear function of H/c that is relatively independent of z_0. This relationship indicated that the stow lift force can be decreased by up to 80% by lowering the stow height of a fixed size panel such that H/c

decreases from 0.5 to 0.2 (Jafari *et al.* 2019a). The pylon height is fixed in contemporary heliostat designs (Pfahl *et al.* 2017a), nevertheless novel concepts such as a carousel heliostat with spindle drive (Pfahl *et al.* 2017b) to lower the heliostat mirror close to the ground in stow during high-wind conditions can reduce the maximum wind loads and the cost of a cantilevered heliostat.

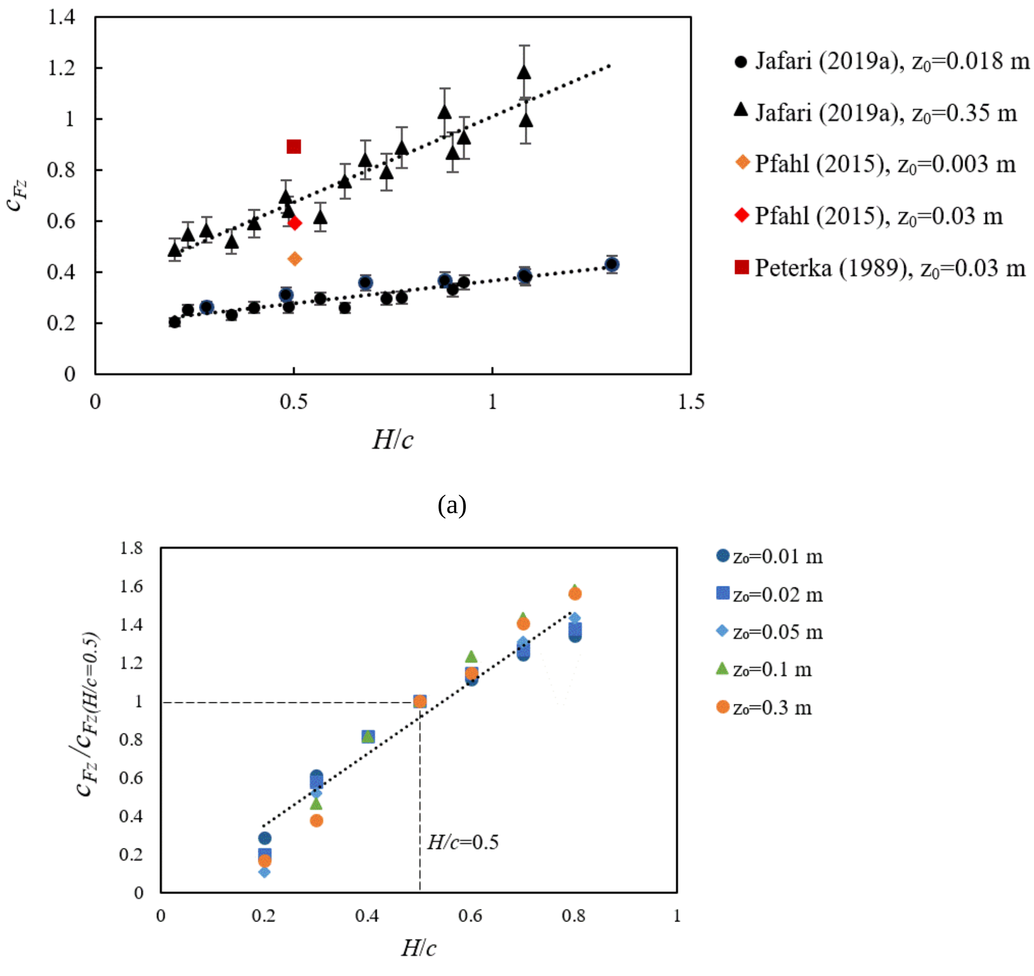

Figure 14. Effect of the hinge height to panel chord length ratio H/c on: (a) the peak lift force coefficient at stow based on different wind tunnel studies, (b) peak lift coefficient normalised with respect to heliostat with $H/c = 0.5$, as a function of ABL aerodynamic roughness height z_0. Reproduced from Jafari *et al.* (2019a).

4. Dynamic wind effects on heliostat vibrations and tracking error

4.1. Heliostat surface pressure distributions

Dynamic wind load analysis on heliostats has been investigated using transient FEA simulations and experimental data from wind tunnel or full-scale measurements, such as through surface pressure measurements by Gong *et al.* (2013) on a 1:10 scale model T-shaped heliostat. Gong *et al.* (2013)

showed that at the leading edge of the stowed heliostat mirror surface, substantial negative peak wind pressure coefficients occurred. It is presumed that the turbulent eddies associated with the peaks of the turbulence spectra that are similar in size to the chord length of the heliostat mirror have a large impact on the maximum lift forces and hinge moments on stowed heliostats (Pfahl *et al.* 2015). However, the effect of the size of these eddies relative to the size of the heliostat chord length on the unsteady loads and non-uniform pressure distributions on stowed heliostats has not previously been investigated.

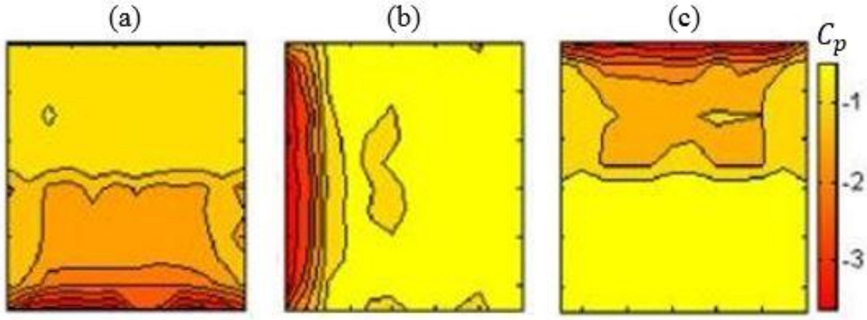

Figure 15. Peak pressure coefficient contours on a stowed heliostat at different azimuth angles: (a) $\beta = 0°$; (b) $\beta = 90°$; (c) $\beta = 180°$. Reproduced from Gong *et al.* (2013).

Pfahl *et al.* (2014b) showed that the temporal variation of the stow hinge moment on an 8 m^2 heliostat, instrumented with 84 differential pressure sensors in an open field in Lilienthal in northern Germany (Figure 16a), exhibited distinctive peaks over consecutive durations of approximately one second. This suggests that the 3-second gust wind speed commonly applied in design codes and standards (ASCE 7-02 2002; EN 1991-1.4 2010; AS/NZS 1170.2 2011) and recommended by the World Meteorological Organisation (WMO) for wind measurements, can under-estimate the gust wind speed and the maximum unsteady wind loads on heliostats. The peak pressure coefficient distribution in Figure 16(b) at the instant of the maximum hinge moment, with peak $c_{MHy} = 0.18$ and $c_{Fz} = 1.0$ at $\beta = 47°$ and $U = 5$ m/s indicates a significant variation of positive pressure (suction) along the side edges. Pfahl (2018) discussed that the peak aerodynamic coefficients showed a general agreement with tabulated values derived in controlled wind tunnel experiments by Peterka and Derickson (1992) at $I_u = 18\%$ and $U = 12.5$ m/s. However, the turbulence characteristics of the ABL flow in the field study by Pfahl (2018) were not reported. Notably the spatial similarity of the heliostat chord length ($c = 2.5$ m) and the integral length scale of the energy-containing turbulent eddies was only estimated as $L_u^x = 3$ m at $z = H = 2$ m, based on extrapolation of semi-empirical data (ESDU 85020 2001) in an open country terrain with $z_0 = 0.03$ m. High-frequency field measurements of wind velocity are thus required to validate the turbulence characteristics at heights below 6 m where heliostats are stowed and verify the peak wind load coefficients corresponding to the critical operating and stow load cases of heliostats established in wind tunnel experiments.

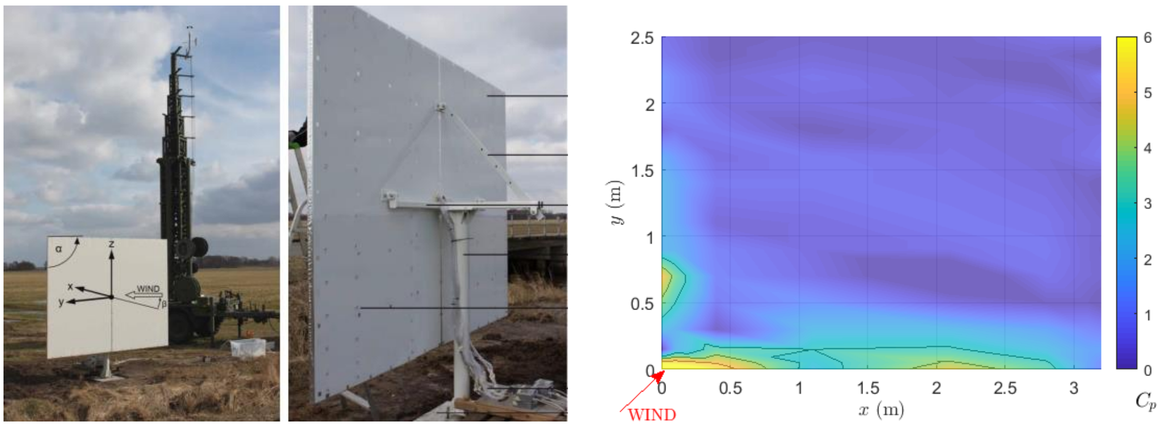

(a) (b)

Figure 16. (a) Field heliostat instrumented with differential pressure sensors in open country terrain (Pfahl 2014a); (b) peak pressure coefficient distribution corresponding to the maximum hinge moment $c_{MHy} = 0.18$ on the stowed heliostat at $\beta = 47°$, reproduced from Pfahl (2018).

Emes *et al.* (2019a) showed that the hinge moment was highly correlated with the movement of the unsteady centre of pressure from the central elevation axis, which increased significantly with increasing turbulence intensity and decreasing elevation angle of the heliostat. Through the decomposition of the hinge moment into the net normal force and the centre of pressure distance, the pressure distributions on the heliostat surface representing the maximum hinge, overturning and azimuth moments were determined (Emes *et al.* 2019b). A high-pressure region was observed on the operating heliostat surface at $\alpha = 30°$ in Figure 17(a), leading to the maximum $c_{Fz} = 2.83$ and $c_{MHy} = 0.18$. Despite smaller peak values of $c_{Fz} = 0.42$ and $c_{MHy} = 0.11$ on the stowed heliostat at $\alpha = 0°$ in Figure 17(b), there was an increased longitudinal (x) movement from the central elevation axis ($y = 0.4$ m) relative to the operating heliostat. During operation, an area of high-pressure difference on the frontal half of the heliostat surface ($\alpha = 30°$) and flow separation at the windward edge of the stowed heliostat surface ($\alpha = 0°$) created the highest hinge moment on the torque tube. In contrast, the maximum azimuth moment during operation (Figure 17c) corresponded to the maximum drag coefficient $c_{Fx} = 2.29$ at $\alpha = 90°$) but with wind approaching the heliostat at $\beta = 60°$. Probability distributions of the transient load fluctuations followed a Gaussian distribution for most of the load cases except the maximum operating azimuth moment (Emes *et al.* 2020a). In contrast, wind tunnel measurements by Xiong *et al.* (2021) found that the fluctuating shear force at the base of the heliostat pylon followed a Gaussian distribution at α between 0° and 20° and the peak value of the base shear force was most accurately represented by a Generalized Pareto Distribution (GPD) at α between 30° and 90°. This suggests that the quasi-steady peak wind loads are generally appropriate to predict the maximum loads in operating and stow configurations, but extreme value analysis of the fluctuating load distribution should be considered in operating positions. It should be noted that despite the smaller peak coefficients on a stowed heliostat, the ultimate design loads should consider a larger survival wind speed compared to the wind speed for calculation of the maximum operating hinge and overturning moments.

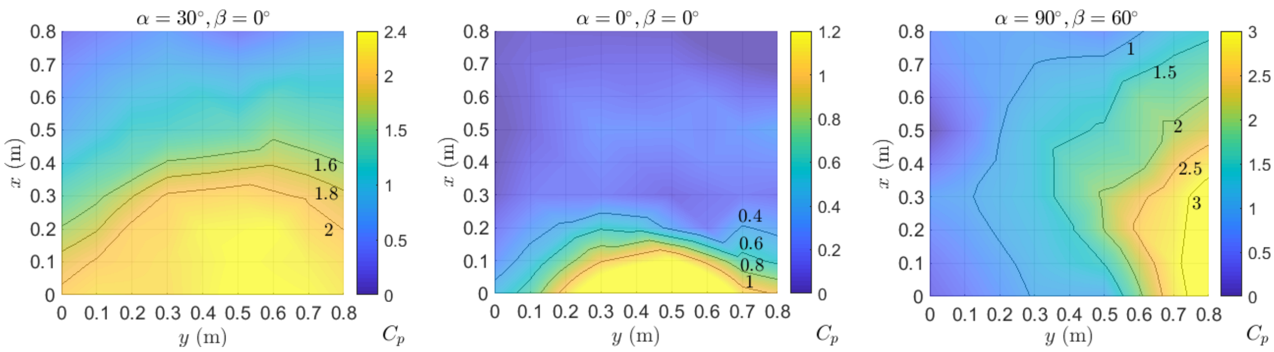

(a) (b) (c)

Figure 17. Peak pressure distributions on an instrumented heliostat in a boundary layer wind tunnel with $I_u = 13\%$ and $I_w = 8\%$, leading to the maximum: (a) operating hinge moment, (b) stow hinge moment, (c) azimuth moment (Emes *et al.* 2019a).

4.2. Modal vibration analysis and fatigue loads

The dynamic response of small-scale structures such as heliostats affects their ability to withstand gusts in the ABL and maintain structural integrity for their expected design life. As heliostats are slender in shape and have low natural frequencies less than 10 Hz, the structural components of heliostats can be exposed to flow-induced vibrations from the unsteady fluctuating loads caused by turbulence effects. Vortex shedding can generate cyclic wind load fluctuations on the elevation and azimuth drives in the frequency range between 1 and 5 Hz of a conventional heliostat, as well as significant vibration and resonance effects (Gong *et al.* 2012; Griffith *et al.* 2015). Excessive deflections and stresses caused by wind-induced oscillations can lead to structural failure (Jain *et al.* 1996; Mendis *et al.* 2007). Galloping and torsional flutter tend to occur at frequencies on the order of 1 Hz where the turbulence integral length scales are similar in size to the characteristic length of the heliostat components, such as the pylon, torque tube and mirror structural truss members. A quasi-steady increase in mean velocity occurs when the turbulence scale is increased beyond the order of magnitude of the body scale (Nakamura 1993) and the galloping effect becomes negligible when the turbulence scale is decreased below the size of the structural member as smaller eddies cannot cause high net pressures over the surface (Pfahl *et al.* 2015).

The equivalent static wind loads have been the subject of most experimental studies, however the dynamic loads due to wind-induced displacements are important for determining the heliostat drive units and support structure components. Dynamic testing of full-scale heliostats was undertaken by Sandia National Laboratories at the National Solar Thermal Test Facility (NSTTF) on a 37 m^2 heliostat instrumented with triaxial accelerometers, strain gauges and anemometers to evaluate the modal shapes and frequencies (Andraka *et al.* 2013). Modal tests of the NSTTF heliostat using hammer excitation identified a number of modes of vibration, including bending of the support structure in modes 1 and 2, bending of the torque tube in modes 3 (Figure 18) and 4, and in-plane and out-of-plane bending of the mirror-truss assemblies (Griffith *et al.* 2012; Ho *et al.* 2012). The natural frequencies derived from experimental measurements showed good agreement with finite element analysis (FEA) predictions of the wind-excited dynamic response, such as a modal frequency of 3 Hz corresponding to the first torque tube bending mode 3 in Figure 18. However, higher order modes with dependence on the stiffness properties of joints and drive mechanisms, such as out-of-plane support structure bending modes, were not accurately predicted by the FEA model. Furthermore, the low-frequency modes of vibration showed increased damping by 24-120% due to aerodynamic damping excited by the wind at speeds of 5-15 m/s compared with the calm winds during the hammer-excited tests. Comparison of the modal frequencies on different heliostat sizes and elevation angles showed that the azimuth drive modal frequency increased from 1.28 Hz to 2.28 Hz at $\alpha = 90°$ and from 1.04 Hz to 1.75 Hz at $\alpha = 0°$ with increasing heliostat size from 37 m^2 to 60 m^2 (Ho *et al.* 2012).

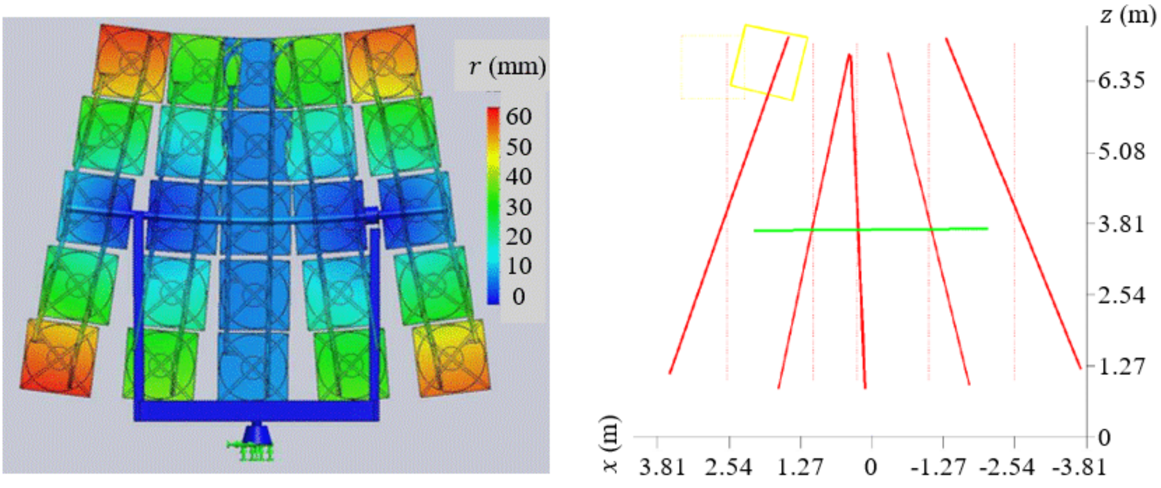

(a) (b)

Figure 18. Heliostat deformed shape for torque tube bending mode 3: (a) FEA simulation of displacement contours with modal frequency of 3.002 Hz, and (b) experimental hammer excitation test with modal frequency of 3.034 Hz. Adapted from Menicucci *et al.* (2012). The red lines represent the deformed experimental mode shape of the five columns from the undeformed reference geometry, the yellow box represents the instrumented facet, and the green line represents the yoke with measurement locations at the endpoints.

Vásquez-Arango *et al.* (2015) validated a finite element analysis (FEA) model with hammer-excited experimental modal data, which showed that the shapes of vibration corresponding to rigid body modes of the mirror frame, such as the oscillation about the elevation axis, were excited by fluctuating wind loads. Admittance functions were applied using spectral analysis of the transient velocity, load and displacements following a normal distribution to predict peak values and standard deviations of moments about principal axes of mirror frame and displacements in the normal direction of the mirror surface. Structural failure through overstressing was evaluated by estimating the maximum stresses on support structure components, such that the maximum displacements due to the dynamic response were calculated to be less than 1% of the heliostat chord length (Vasquez Arango *et al.* 2017).

Dynamic wind loads on heliostats have been investigated by fluid-structure interaction (FSI), combining transient CFD, FEA simulations and modal analysis to link the resolved flow field with the structural response. A FSI analysis by Vasquez Arango *et al.* (2017) showed a pronounced peak at $f = 3.8$ Hz in the spectral distribution of the overturning moment coefficients on a 2.5 m × 3.22 m heliostat model. In comparison, spectral analysis of the fluctuating azimuth and overturning moments on a 0.8 m square heliostat model by Emes *et al.* (2020b) in a boundary layer wind tunnel experiment showed a clearly defined peak at $f = 7$ Hz. Wolmarans and Craig (2019) performed a one-way FSI modal analysis with scale resolving CFD simulation of a full-scale heliostat to determine the location of maximum stress at two elevation angles. As shown in Figure 19(a), the maximum von Mises stress occurred near the base of the LH-2 heliostat on the back face of the pylon. The dynamic behaviour consisted of back-and-forth motion of the concentrator due to the large bending moment caused by the maximum frontal area to the oncoming wind at $\alpha = 90°$. In contrast, the maximum induced stress decreased and was located at the T-joint between the torque tube and the pylon at $\alpha = 30°$ in Figure 19(b). Spectral analysis of the fluctuating stresses indicated dominant frequencies in the 6 Hz range corresponding to the modal frequencies, with increasing side-to-side and flexural motions of the concentrator at $\alpha = 30°$ caused by the peak hinge moment about the torque tube. Although coupled or two-way FSI using LES is a promising method to investigate dynamic wind loads on heliostats, the computational effort with increased accuracy models is very high (Pfahl *et al.* 2017a; Wolmarans and Craig 2019). Consideration of the dynamic amplification of the load fluctuations on the heliostat components requires further investigation to understand the conditions that promote the coupling effects between ABL turbulence and modal frequencies of the structure.

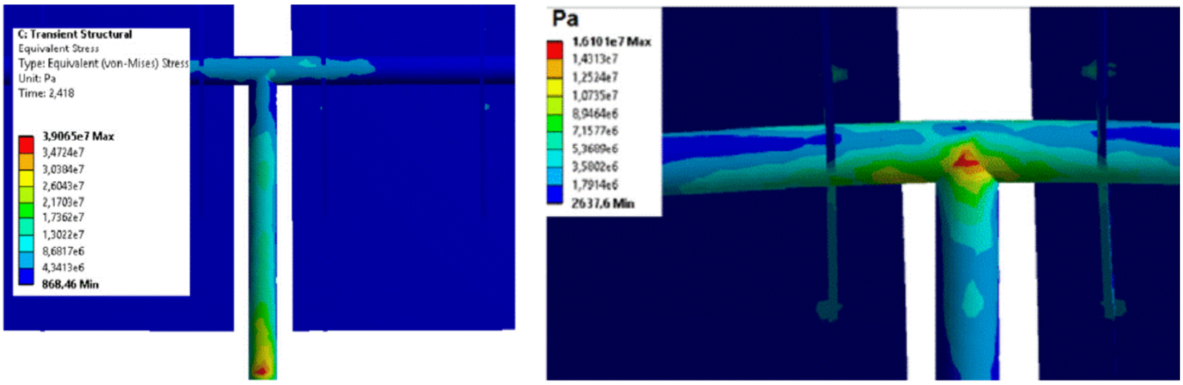

(a) (b)

Figure 19. Maximum von Mises stress contour from a one-way FSI modal analysis of the LH-2 heliostat at (a) $\alpha = 90°$, and (b) $\alpha = 30°$ (Wolmarans and Craig 2019).

4.3. *Wind-induced tracking error and operational performance*

Ho *et al.* (2012) investigated two rigid-body vibrational modes at 1-2 Hz of the 37 m^2 NSTTF heliostat correlating to backlash of the elevation and azimuth drives in a field experiment test at Sandia National Laboratories (Ho *et al.* 2012; Griffith *et al.* 2015). Furthermore, hammer-excited experimental modal analysis showed that the truss member to torque tube interfaces due to out-of-plane bending modes (Figure 20) were most vulnerable to wind-induced stresses. Maximum beam deviations of 0.17 m and 1.58 m in the horizontal and vertical directions were observed on the tower target, compared with deviations of 0.1 m and 0.25 m due to gravity in the absence of wind (Ho *et al.* 2012).

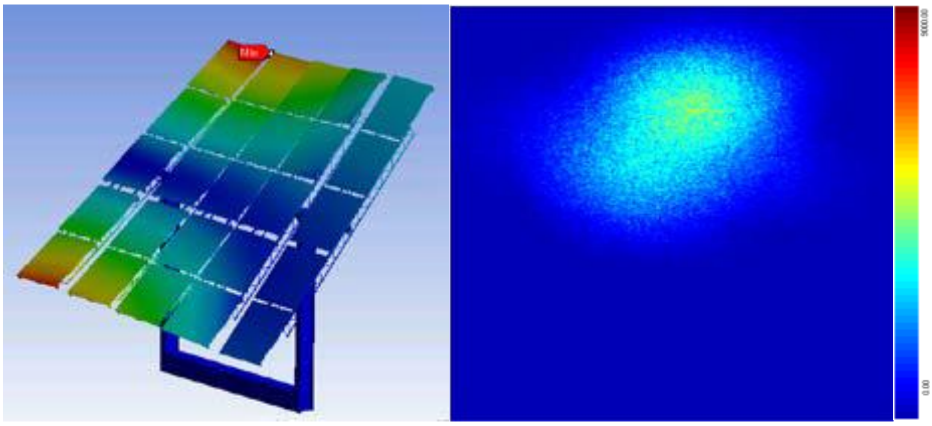

Figure 20. Heliostat deformed shape for out-of-plane bending mode 2 due to wind excitation that can impact optical performance through deviation of the beam centroid (Ho *et al.* 2012).

Dynamic photogrammetry measurements on the 48.5 m^2 Stellio heliostat by Blume *et al.* (2020) revealed that the wind-induced tracking deviation of 0.44 mrad RMS (Figure 21a) contained a resonant component RMS value an order of magnitude smaller than the combined RMS values of the mean and background components. This tracking deviation caused by the wind contributed to approximately one third of the typical total tracking deviation of heliostats. Wind-induced oscillations and deformations at frequencies below 4 Hz in the amplitude spectra (Figure 21b) most significantly impacted the optical performance of the heliostat at a mean wind speed of 4.8 m/s and turbulence intensity of 26% (Figure 21c). To complement the relationships between quasi-static peak wind loads and ABL turbulence in Section 2, spectral analysis correlations between the fluctuating components of the wind velocity and the resonant component of the tracking deviations in field investigations would provide a further insight into the wind-induced oscillations that impact the operational performance of a range of full-scale heliostat prototypes.

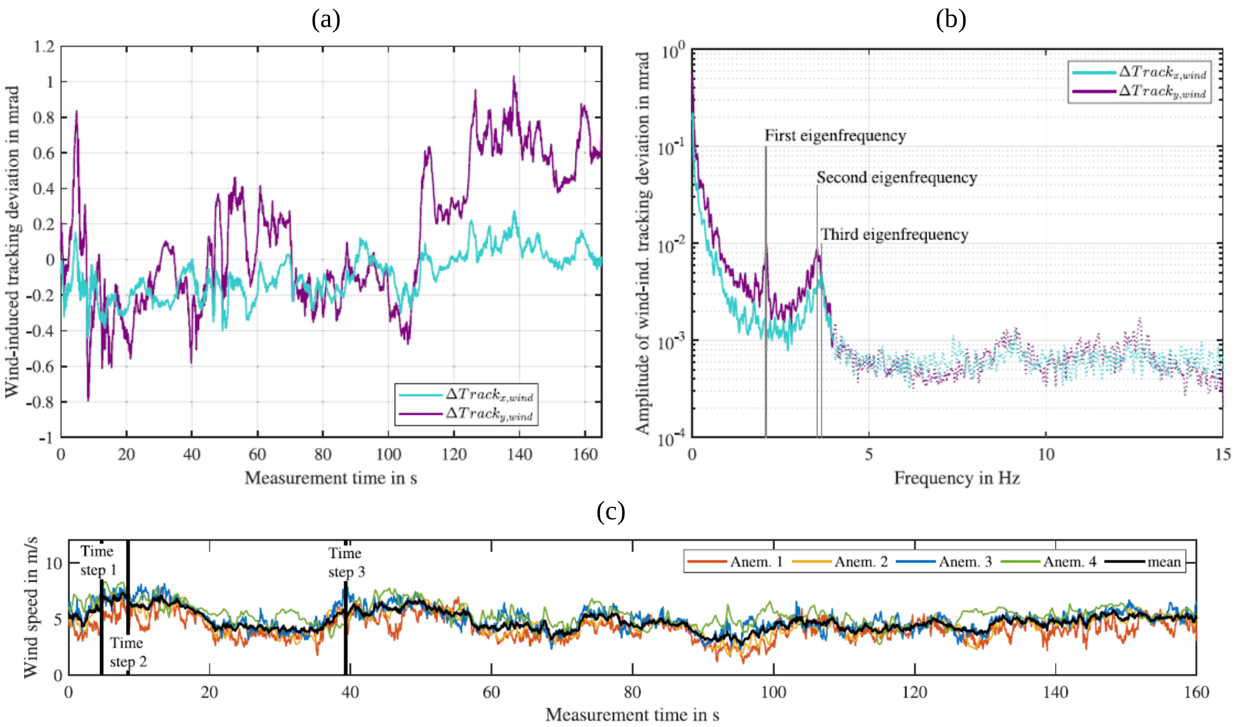

Figure 21. (a) Time history of the wind-induced tracking deviation in the lateral (x) and longitudinal (y) directions of the Stellio heliostat concentrator at $\alpha = 45°$ and $\beta = 76°$; (b) amplitude spectra of the wind-induced tracking deviations with a low-pass filter and cut-off frequency of 4 Hz; (c) time history of wind speed averaged over four ultrasonic anemometers on measurement mast at the Jülich DLR field site (Blume *et al.* 2020).

5. Aerodynamics of a heliostat field

Heliostat fields are arranged in rows in a radial (Figure 22a) or polar (Figure 22b) configuration surrounding a central tower. For an optimum optical performance, the radial distance between the rows in a heliostat field typically ranges between a value larger than the chord length of the mirror panel, x/c >1 in the inner field rows, to x/c=8 at the perimeter of the field(Hui 2011). Heliostats close to the tower have field densities greater than 40% with smaller shading effects and are typically spaced less than 20 m apart for a typical heliostat mirror area of 120 m^2 (Noone *et al.* 2012). With increasing distance from the central tower, the field density decreases to less than 20% and spacing between heliostats of up to 45 m at the outer boundary of the field (Pfahl *et al.* 2011c; Noone *et al.* 2012). The layout of heliostat fields in power tower plants has been optimised disregarding of wind load and primarily with respect to the optical efficiency of the field. However, static wind loads on tandem heliostats are strongly dependent on the spacing between the heliostat mirrors, defined by the gap ratio x/c and the heliostat field density defined as the ratio of mirror area to land area. As wind flows over a heliostat, a region of disturbed flow is created downstream in its wake. Within the field, the mean flow and turbulence characteristics might be significantly different from the incoming ABL and thus alter the wind loads on heliostats in the field from those on a single heliostat. Hence, wind loads on heliostats at different in-field positions could be evaluated given knowledge of differences in flow and turbulence characteristics within a field. This provides a chance to optimise the design and cost of a heliostat field, with respect to the inner flow field aerodynamics represented by a combination of ABL turbulence and upstream heliostat wake-generated turbulence.

(a) (b)

Figure 22. Different layouts of a heliostat field. (a) A radial heliostat field, Noor III in Morocco. Image from www.masen.ma, (b) a polar heliostat field, PS10 in Spain. Image from www.eusolaris.eu.

5.1. Heliostat wake measurements

Flow around a heliostat, in the absence of the support structure and the pylon, is resembled by flow around a thin flat plate. As flow passes around a thin flat plate, it separates from the plate at its edges and a low-pressure region is formed in its immediate downstream. The separated shear layers then roll up into large scale vortices shedding into the wake. Blockage of the flow by the plate and vortex shedding in the wake lead to a reduction of mean velocity and an increase in turbulence intensity. The alternate shedding of the rolled-up shear layers into the wake creates oscillations in the flow, characterised by the dominant frequency of vortex shedding. The aerodynamics of multiple heliostats differ from a single heliostat due to the interference of their wakes with each other and the interaction of the downstream heliostats depending on their arrangement and spacing between them.

The profiles of mean velocity and turbulence intensity of the approaching boundary layer were characterised by Sment and Ho (2014) using three tri-axial ultrasonic anemometers mounted on a weather tower upstream of a row of instrumented heliostats. Anemometers were also mounted on the heliostats and on portable towers between five rows of the NSTTF heliostat field to measure of the turbulence statistics of the flow in the vicinity of the heliostats. Figure 23 shows that an increase of turbulence intensity to more than 50% downstream of the first and second row of heliostats at $\alpha = 90°$ (vertical) and 45°. For the heliostats in stow (not shown) however, turbulence intensities showed only a small variation in downstream rows and remained below the maximum turbulence intensity of 20% approaching the outer row of the field (Sment and Ho 2014).

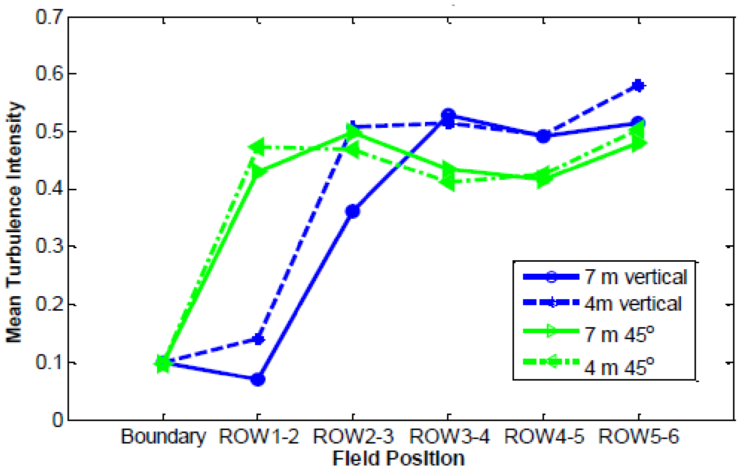

Figure 23. Turbulence intensity in different rows of a heliostat field as a function of heliostat elevation angle. Sment and Ho (2014).

Within the boundary layer, the variable shear and turbulence in affect the development of the wake of a heliostat and the turbulence structure in its wake significantly. Jafari *et al.* (2020a) conducted velocity measurements in the wake of a heliostat model placed in simulated atmospheric boundary layers in the wind tunnel to characterise the turbulence variations in the heliostat wake. It was found that in the wake of a heliostat, the turbulence properties were significantly different from the atmospheric boundary layer. The results showed a reduction in mean velocity in the wake, which did not recover over the measured downstream distance up to $x/c = 8$. This was accompanied by an increase in turbulence intensity up to $x/c = 4$, with a peak at approximately $x/c = 1.5$ where the streamwise and vertical turbulence intensities increased by more than 12-times their incoming values at elevation angles of 60° and 90°. Furthermore, it was found that in the wake immediately downstream of the heliostat, the length scales of turbulence were significantly smaller as the large inflow turbulence length scales were broken into smaller scales.

The variations of turbulence intensity in the heliostat wake at different streamwise distances indicates the impact of field density on heliostat wind loads. For example, due to the higher turbulence intensity caused by the heliostat wake, the unsteady wind loads in high-density zones of a heliostat field at $x/c = 1 - 3$ are greater than in low-density zones. This shows the impact of dynamic wind loads for design of heliostats as they are likely to influence the dominant frequencies of the unsteady and dynamic loads on heliostats in dense zones of a field. Furthermore, despite the reduced mean wind speed within the field, static wind loads such as the hinge moment may increase within the field depending on the field density and the elevation angle of heliostats during operation.

5.2. Loads in heliostat field arrays

The review of the aerodynamics of tandem flat plates and side-by-side flat plates shows that the wake flow around multiple heliostats and thus the wind loads on in-field heliostats can differfrom those on a single heliostat. One of the critical parameters that influences the wind loads is the non-dimensional gap in the longitudinal direction with respect to the mirror chord length, x/c, between the heliostats in an array. Emes *et al.* (2018) investigated the variation of the stow wind loads on two tandem heliostats and showed that the peak lift force coefficient on the second tandem heliostat in stow was up to 7% larger than that for the single stowed heliostat for $x/c > 1.5$. As shown in Figure 24, Jafari *et al.* (2020b) found that the peak hinge moment coefficient on a tandem heliostat increased to 1.5-times that on a single heliostat at elevation angles of 30° and more than double at elevation angles of 60° and 90°. Despite the lower mean pressure coefficient on the tandem heliostat, a region of large-magnitude peak pressure existed at the leading edge of the panel. Furthermore, analysis of the unsteady pressure distributions showed an increased unsteady centre of pressure variation on the second tandem heliostat, specifically at elevation angles of 30° and 60°. The unsteady variations of the position of the centre of pressure as a result of the larger turbulence intensity in the wake were found increase the mean and peak hinge moment coefficients on the second heliostat. The large increase of the hinge moment coefficient can outweigh the reduced wind speed in the wake with respect to the gap between the heliostats and the elevation angle of the heliostat panel. For example, at an elevation angle of 30° and x/c between 4 to 8, the mean wind speed reduced by less than 10%, while the hinge moment coefficient was 50% larger than the single heliostat, leading to an increase of between 20% and 50% in the peak hinge moment. Hence, the results highlight an opportunity to modify the heliostat design for in-field heliostats compared to field-edge heliostats.

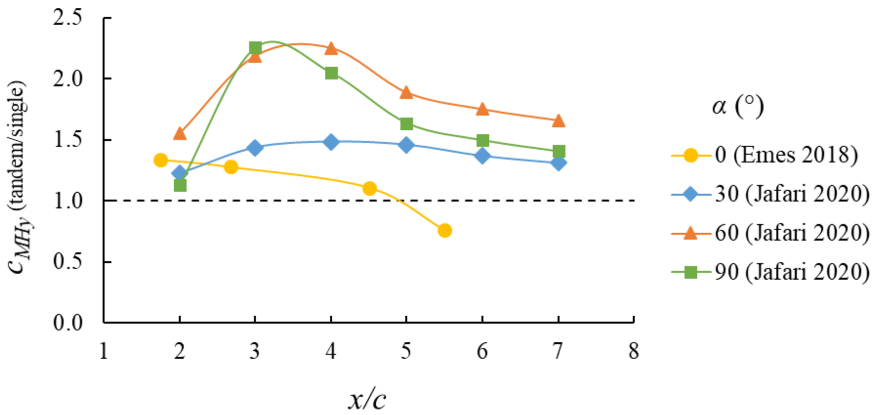

Figure 24. Peak hinge moment coefficient on a tandem heliostat normalised to a single heliostat as a function of longitudinal gap spacing x/c between tandem heliostats at elevation angle α (Emes *et al.* 2018; Jafari *et al.* 2020b).

In the literature, wind tunnel studies have been performed to study the influence of fences on the wind loads on heliostats in field arrangements. . Peterka *et al.* (1986) measured the wind loads on a heliostat placed in an array with perimeter and in-field fences. The configuration of the heliostat array was chosen based on different regions of a field with different densities. Fences with porosities of 0.4, 0.5 and 0.6 and two heights, equal to 0.9 and 1.35 times the heliostat hinge height, were investigated. They found that with addition of the fence, the mean drag force coefficient on a heliostat at α =90° and a wind direction of 250° in the third row of an array was reduced from approximately 1 to 0.45. The results in Figure 25(c) were presented as a function of generalised blockage area (GBA), defined as the ratio of the area of upstream blockage projected to wind direction, including external and internal fences and upstream heliostats, over the field ground area. Peterka *et al.* (1989) reports the ratio of the peak drag and lift force coefficients in a field as a function of GBA as shown in Figure 25(a–b). The results show cases where the peak coefficients are larger than a single heliostat, shaded by red in Figure 25(a–b). The reason for increase of wind loads was not explained by Peterka *et al.* (1986). Furthermore, the elevation angles and heliostat configurations for the presented results were not provided, and it is not clear for which conditions the wind loads were larger than a single heliostat. Moreover, the results were only presented as a function of GBA, which includes the effects of both the fence and blockage by upstream heliostats. Hence, the influence of the fence on the wind loads was not distinguished.

Peterka *et al.* (1987) measured the wind loads on 1:60 scale-model heliostats in the fourth row of a four-row arrangement for two different gap ratios between consecutive rows, x/c =6.4 and x/c =3.07, representing low- and high-density zones of a heliostat field. The mean drag force coefficient of a fourth-row heliostat was found to be 12% lower than that of a front-row heliostat at x/c =3.07. For a higher field density, the reduction in the mean drag coefficient increased to only 32% of that in the first row. In contrast, the peak drag force coefficient on of a fourth-row heliostat with $x/c = 6.4$ was found to be 40% larger than that of a front-row heliostat. Pfahl *et al.* (2011c) measured the wind loads on 1:20 scale-models of a four-row tandem arrangement with 30 m^2 mirror area for field densities of 10% and 50% corresponding to gap ratios (x/c) between the mirrors of 5.5 and 1.5, respectively. Peterka *et al.* (1987) and Pfahl *et al.* (2011c) found up to 50% reduction in peak drag and lift forces on a second heliostat at $\alpha = 90°$ compared to the front-row heliostat in a tandem arrangement at a field density of 50%. The larger peak drag coefficient may be correlated with an increase in longitudinal turbulence intensity of the flow, however the relative contribution of the longitudinal and vertical turbulence components to the lift and hinge moment coefficients on operating heliostats has not been determined. This highlights the importance of characterisation of turbulence in the wake of heliostats and its effect on the wind loads, and measurement of wind loads in a field. Understanding the variations of wind loads within a heliostat field can help to improve the field design with respect to the wind loads. For regions of a field with reduced wind speed and increased turbulence intensity, the structural stiffness and foundation depth of heliostats can be decreased if the dynamic loads are not overcompensated by an increase in unsteady wind loads.

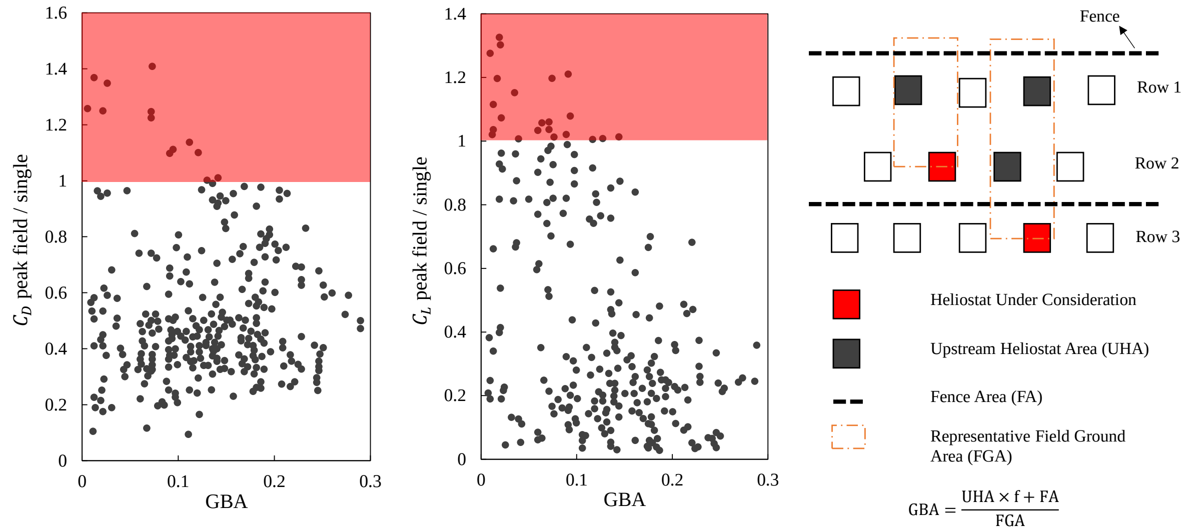

(a) (b) (c)

Figure 25. (a) Peak drag and (b) peak lift force coefficients in an array with perimeter and in-field fences normalised with the peak force coefficients on a single heliostat as a function of generalised blockage area, GBA. The red shaded regions show cases where the peak wind load coefficients are larger compared to a single heliostat. (c) A schematic of the heliostat array demonstrating the calculation of GBA. Reproduced from Peterka *et al.* (1989).

In a similar experiment, Pfahl (2018) measured the wind loads on a heliostat in the fourth row of an array in presence of a fence upstream of the first row. The fence had a porosity of 40% and height equal to 1.25 times the heliostat hinge height. Different cases with varied distances between the heliostat rows and between the fence and the front row were investigated, through which GBA varied between 0.053 and 0.46. Their results in general showed that the maximum wind load coefficients at operating elevation angles were less than a single heliostat for the investigated range of GBA. As shown in Figure 26, the peak lift force coefficient on a stowed heliostat was up to 25% larger than a single heliostat for GBA values less than 0.1. The increase in the stow lift force coefficient was suggested to be related to an increase in vertical velocity component downstream of the fence. If the entire field is to have a consistent heliostat design, according to Pfahl (2018), application of fences therefore may not be beneficial due to the increase of the lift force in stow position and the negligible impact of the fence on low density regions of the field. As the results were presented as a function of GBA, the effect of fence was not differentiated from the effect of blockage by heliostats at the upstream rows. Pfahl (2018) discussed that the uncertainty in the reported results was large due to the limited measurement cases.

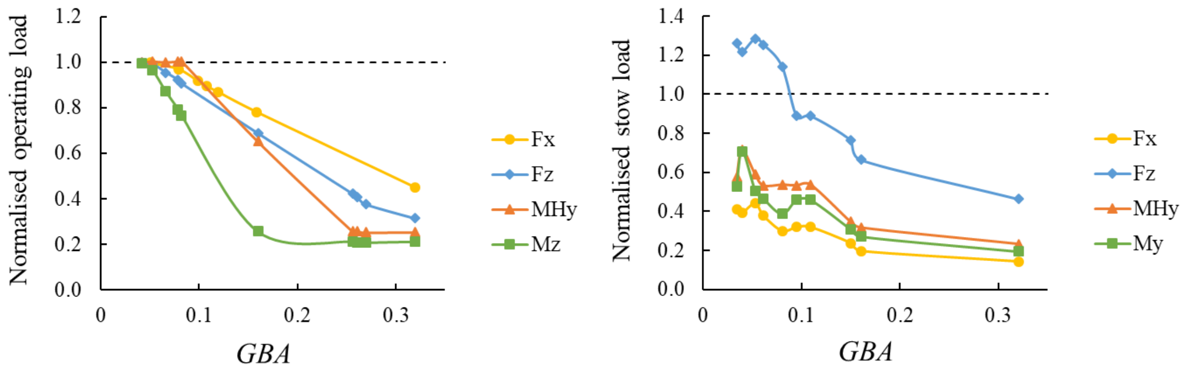

(a) (b)

Figure 26. Peak aerodynamic coefficients as a function of GBA, normalised with respect to $GBA = 0$ for an isolated heliostat in (a) maximum operating position (Peterka and Derickson 1992); (b) stow position (Pfahl 2018).

5.3. Wind load mitigation techniques

The wind load reduction on in-field heliostats in wind tunnel experiments by Peterka *et al.* (1986) and Pfahl (2018) compared to a single heliostat were presented as a function of GBA, such that the effects of both the fence and blockage by upstream heliostats were not distinguished. Hence, the manipulation of inflow ABL turbulence by the fence and its effectiveness in wind load reduction were not reported. Turbulence properties downstream of mesh fences (Figure 27b) of various mesh opening widths and porosities were determined from experimental measurements in a wind tunnel (Jafari *et al.* 2021). It was found that with application of fences with porosities between 0.46 and 0.75, an inflow streamwise turbulence intensity of 12.5% could be reduced to between 8.8% and 9.9%. Furthermore, a significant reduction in the integral length scale of turbulence was shown immediately downstream of the fences and grew afterwards with increasing the downstream distance, with the longitudinal length scale remaining 25% and the vertical length scale remaining 21% below the inflow level for the fences with porosities between 0.46 and 0.64. Through comparison of the turbulence reduction behind wire mesh fences with different porosities and mesh opening widths, it was found that porosity was the main factor which determined the reduction in turbulence intensity and length scales. Based on the variation of mean velocity, turbulence intensity and integral length scale behind the fences, it was estimated that the peak drag force on a heliostat at the vertical position could be reduced by 48% with utilisation of a wire mesh fence with a porosity of 0.46 using the developed relationships in Jafari *et al.* (2018). it was predicted that the peak lift force on a stowed heliostat could be reduced by 53% behind a wire mesh fence with a porosity of 0.46 based on the correlation given in Jafari *et al.* (2019a), as shown in Figure 27(b). With increasing the porosity of the wire mesh fence to 0.75, the reduction in peak drag and lift forces could only reach 19% and 15%, respectively. The measurement of forces on a heliostat behind the fence can further verify these estimated peak load reductions derived from the turbulence intensities and length scales reductions due to the fence. For such a method to be employed in a heliostat field, further study is necessary in the future. to determine the optimum geometric parameters of the mesh fence, including its height and distance to the heliostats.

Wind load reduction by fences may be more appropriate for heliostats of smaller dimensions, due to the increased material cost of larger fences that would be required for a field of large-scale heliostats. Although fences at the perimeter of the field have been shown to have negligible impact on the forces on heliostats with increasing distance into the field, a modification in the design of perimeter fences to heliostat edge-mounted devices may reduce the wind loads on in-field heliostats. The high overturning moments on a stowed heliostat are due to the vertical velocity component of the turbulent flow separating at the leading edge, which creates suction on the other side of the mirror and a high-pressure difference between the upper and lower heliostat surfaces. Wind tunnel experiments by ToughTrough indicated that fence-like "spoilers" (Figure 27a) can reduce separation and suction near the leading edge in stow position, leading to 40% wind load reduction and 30% weight reduction of heliostat support structure (Pfahl *et al.* 2014b). A disadvantage of such flow manipulator devices is the additional maintenance cost to clean the mirrors and the shading of the mirrors.

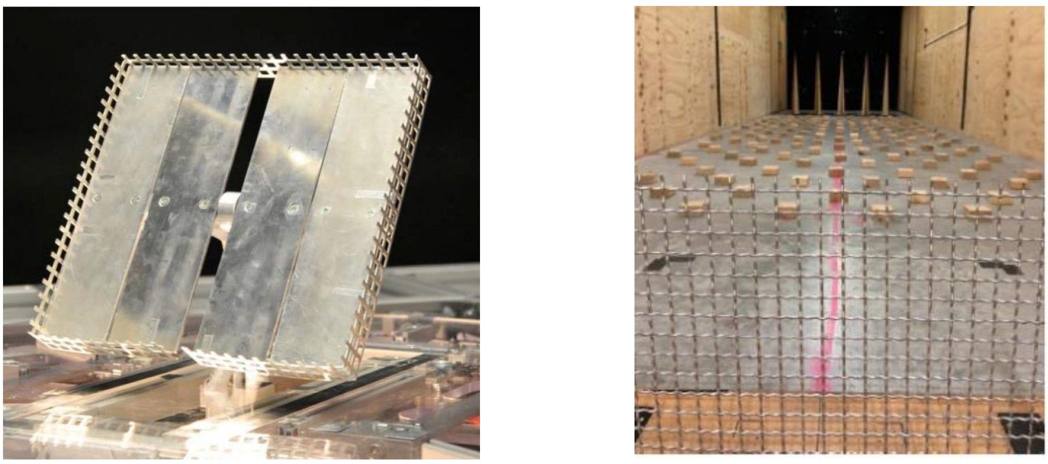

(a) (b)

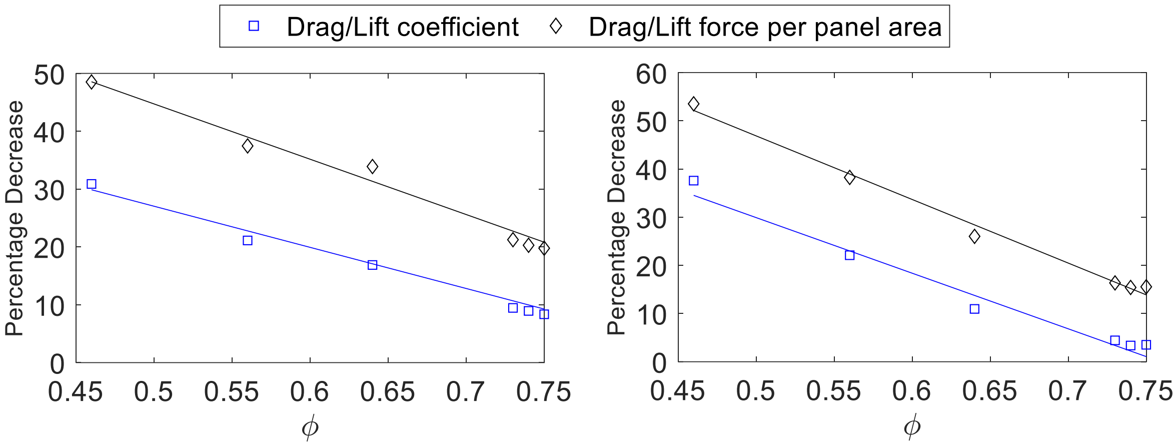

(c) (d)

Figure 27. Wind load mitigation techniques using (a) heliostat edge-treatment devices (Pfahl *et al.* 2013), and (b) a heliostat field perimeter porous wire mesh fence (Jafari *et al.* 2021). The plots show the effect of wire mesh fence porosity on the predicted reduction of (c) the peak drag force/coefficient on a heliostat at $\alpha = 90°$, (d) the peak lift force/coefficient on a heliostat at $\alpha = 0°$ (Jafari *et al.* 2021).

6. Discussion

6.1. Resolution of heliostat field measurements in plant performance models

Typical meteorological year (TMY) data contains wind and solar radiation data averaged over a duration of one hour as an input to annual solar field efficiency models. In practice during operation of a power tower field, however, heliostats are stowed based on a 3-second gust wind speed (Price *et al.* 2020). Second-generation heliostats were defined by Murphy (1980) with specifications for gust wind speeds of 22 m/s and 40 m/s at a 10-m height for the maximum operational and stow survival design conditions, respectively. This is the same as the 3-second gust wind speed stated in design wind guidelines and norms for buildings and other physical structures with natural frequencies smaller than 1 Hz at a height of 10 metres. Standard wind velocity data at automatic weather stations (Bureau of Meteorology 2020; National Climatic Data Center 2020) are not obtained at a sufficient frequency to reliably determine the longitudinal and vertical turbulence intensities that impact the maximum heliostat wind loads (Blackmon 2014). Long-span cable-supported bridges are sensitive to peak gusts of a duration of the order of 2-3 seconds (Xu 2013), whereas stowed heliostats are exposed to shorter duration gusts of approximately 1 second (Pfahl 2018). Hence, it is expected that the relevant gust period for a heliostat is shorter than that of a building and thus the dynamic response and vibrational mode shapes of heliostats are different. The collection of high frequency (i.e. second) wind velocity and solar radiation data at concentrating solar power plant sites over an extended duration (e.g. years) would increase the accuracy of annual field efficiency models through an improved resolution of operating load data. The transient nature of the ABL should therefore be accounted for in the design of a heliostat field, including the wind load predictions and the assessment of operational performance models.

6.2. Assessment of critical aerodynamic load cases of a heliostat

Design wind load codes and standards provide aerodynamic shape factors, external pressure coefficient and design external pressure, aerodynamic (drag) force coefficient c_F and the centre of pressure distance l_{px}/c from the windward edge of simple-shaped structures based on a characteristic length c of the structure. For example, *Chapter 5 - Wind Loads* of ASCE 7-02 (2002) provides a range of tables containing the design pressures for solid freestanding walls, solid signs and monoslope roofs with tilt angles 10-30° (in increments of 5°) and aspect ratio of the cross-sectional roof area varying between 1/5 and 5. Furthermore, the IEC 61400-1 (2005) wind turbine design standard provides guidance on the static and dynamic loads on wind turbine components, considering the effects of turbulence intensity and length scales and the variation of average and gust wind speeds across the rotor plane. However, heliostats have a non-standard shape that does not conform to conventional shapes of buildings (ASCE 7-02 2002; EN 1991-1.4 2010; AS/NZS 1170.2 2011) and rooftop solar panels (ASCE/SEI 7-16 2016) associated with corner vortices and separation at the leading edge of the building roof (Kopp *et al.* 2012). The thin plate and tubular geometries of heliostat facets, support beams, torque tube and pedestal are not applicable to the design procedures outlined for buildings and wind turbines in terms of their size, shape and position within the lowest 10 m of the ABL. This can lead to under-estimation of the peak loads on heliostats, such as in stow position due to the large dynamic response caused by near-surface gust events (Durst 1960; Mendis *et al.* 2007).

Table 2 shows the maximum operating wind load configurations, in terms of the elevation and azimuth angles that result in the peak wind load coefficients reported in wind tunnel measurements in Table 1 (refer to Section 2.2). For wind approaching an upright heliostat at $\alpha = 90°$ from the front

($\beta = 0°$) or back ($\beta = 180°$), the maximum drag force F_x on the concentrator leads to the maximum overturning moment M_y at the base of the heliostat pylon for design of the foundation. Similarly, on a heliostat inclined at $\alpha = 30°$, the maximum lift force on the heliostat panel leads to a maximum hinge moment M_{Hy} about the elevation axis of the heliostat in operation that impacts the design of the torque tube and elevation drive. The maximum load case for the azimuth drive is the moment about the vertical axis of an upright operating heliostat ($\alpha = 90°$) with wind approaching from an oblique angle $\beta = 60°$ and 120°. The wind load coefficients found by Peterka *et al.* (1989) apply to one case of the ABL with limited information on the turbulence spectra and length scales, particularly in the vertical turbulence component that is crucial to the maximum wind loads in stow position. The maximum wind loads on heliostats often considered wind impacting the front of the heliostat at $\beta = 0°$, however the maximum wind loads on a heliostat at $\beta = 180°$ can be larger and the presence of an upstream heliostat influences the spectral peak of pressure variations in operating positions. (Yu *et al.* 2019). The number of working conditions for azimuth-elevation heliostat configurations can be reduced from 130 to 13 through the application of uniform design method and regression analysis to all wind load coefficients (Xiong *et al.* 2019). The contribution of spectral energy in the turbulent eddies to wind loads and the resulting aerodynamic effects on heliostat geometry over a larger range of orientations has been investigated in more detail in recent wind tunnel experiments (Pfahl *et al.* 2015; Emes *et al.* 2017; Emes *et al.* 2019a; Jafari *et al.* 2019a).

Table 2. Critical operating load cases of an azimuth-elevation heliostat.

Maximum aerodynamic coefficient	α (°)	β (°)
F_x, M_y	90	0, 180
F_z, M_{Hy}	30	0, 180
M_z	90	60, 120

Prediction of the design loads on heliostats should allow for the maximum operating cases and stow cases, due to both the scaling parameters of individual components and the level of ABL turbulence represented by the surrounding terrain. The influence of the heliostat concentrator aspect ratio (Pfahl *et al.* 2011a) and the pylon height (Emes *et al.* 2017; Jafari *et al.* 2019a) have a large effect on the maximum aerodynamic coefficients, whereas small gaps between mirror facets have a negligible impact on the pressure distribution and the wind loads (Wu *et al.* 2010). Structural reliability of the heliostat components through stress analysis by (Benammar and Tee 2019) suggested that the thickness of the pedestal and torque tube can be reduced for operating conditions at low wind speed sites, whereas the torque tube is a critical component that can lead to structural failure in stow position at increased wind speeds. Wind tunnel experiments have shown that for measurement of the unsteady drag force on a heliostat at $\alpha = 90°$, similarity of the streamwise velocity spectrum is required and a model with larger dimensions (i.e. smaller scaling ratio) can be used. In contrast, accurate measurement of the unsteady lift force on a stowed heliostat requires similarity of the vertical turbulence spectrum, which can only be achieved for a model with smaller dimensions or larger scaling ratio (Jafari *et al.* 2019b). The relative contribution of the longitudinal and vertical components of turbulence, for a stowed heliostat and over the range of heliostat operating conditions with varying gap between the lower heliostat edge and the ground, should be further verified through wind tunnel and full-scale measurements. Analysis of wind loads on full-scale heliostats with respect to the incoming wind turbulence measured simultaneously can verify the scaling effects observed in wind tunnel experiments to provide a more reliable estimation of wind loads.

6.3. Modal analysis of heliostat vibrations and wind-induced displacements

Measurements of local deformations and displacements on full-scale heliostats have provided an insight into the dynamic wind loads, such as vibrations and fatigue loads on drive units and support structure components. Modal analyses have been conducted in the literature both computationally and experimentally to determine the mode shapes and frequencies of a heliostat structure. Low-frequency vibrational modes corresponding to quasi-static sway motion of the heliostat subjected to time-averaged loads can be accurately reproduced by numerical simulations. However, modes that are dependent on the stiffness and damping of joints, such as elevation and azimuth drives, are most accurately characterised through full-scale experiments and two-way fluid-structure interaction that captures the gust spectrum range (~1-2 Hz) of the fluctuating load distribution caused by backlash or slop in the gear drives (Griffith *et al.* 2012; Ho *et al.* 2012). High-amplitude dynamic response of the pylon and support structure was less likely to be impacted by the shedding of vortices from the heliostat structure

(Wolmarans and Craig 2019), although this applies to a broad range of frequencies depending on the wind speed and the heliostat size (Ho *et al.* 2012). Hence, the heliostat structure should be designed to avoid wind loads that cause high-amplitude or high-cycle counts in the drive components that result from resonant effects due to convergence of the modal frequencies with the gust frequencies of energy-containing eddies in the approaching wind and the vortex shedding frequency from upstream heliostats. Further work is still necessary to examine dynamic wind loads on heliostats positioned inside the heliostat field. For instance, field measurements can provide validation points to complement numerical studies to investigate load amplification factors associated with different operational wind speeds and turbulence characteristics over an increasing range of heliostat orientations and structural designs.

6.4. Dynamic wind effects on operational heliostat tracking error

Wind engineering design standards do not account for the dynamic effects of heliostats, such as a dynamic response or amplification factor in AS/NZS 1170.2 (2011) for slender buildings and large permanent structures ($H \leq 200$ m) with natural frequencies less than 1 Hz. To avoid structural excitation due to buffeting and torsional galloping, the natural frequency of a long inclined flat plate (i.e. solar array) is recommended to be greater than 5 Hz. Hence, the essential scaling parameters of the heliostat structure and the aerodynamic loads on the tubular components were shown to be very sensitive to the high turbulence in the ABL. Although square-mirrored heliostats are less likely to be exposed to torsional vibrations, the ratio L^x/c of the integral length scales in the longitudinal and vertical directions to the heliostat chord length significantly affects the peak wind loads on heliostats in operating and stow positions (Emes *et al.* 2017; Jafari *et al.* 2019a). Based on the common sizes of heliostat mirrors that are currently manufactured, $L_u^x/c \approx 6.5$ in an open country terrain with $z_0 = 0.03$ m (ESDU 85020 2001). However, L_u^x/c decreases with increasing surface roughness to $L_u^x/c = 5.5$ at $z_0 = 0.05$ m and $L_u^x/c = 4.5$ at $z_0 = 0.1$ m. To reduce the maximum wind loads as L_u^x/c and L_w^x/c approach unity, a heliostat of fixed mirror chord length can be stowed at a lower elevation axis height H that is closer to the ground (Pfahl *et al.* 2017b) through a reduction of H/c and L_u^x/c.

6.5. Variation of wind loads on heliostats throughout a field

Due to the variation in heliostat orientations across a field with respect to the wind, the aerodynamic loads on some heliostats in favourable orientations can be reduced with respect to the maximum load cases in the field. Statistical correlation of wind speed and DNI data with heliostat tracking angles at the Plataforma Solar de Almeria (PSA) CESA-I field by Emes *et al.* (2020c) indicated that a stowing strategy based on wind speed and direction can increase the annual operating time of the heliostat field by 6% with increasing stow design wind speed from 6 m/s to 12 m/s. For an assumed 10-minute stow transition from operating positions of the heliostat field, a stowing strategy that allowed "protected" heliostats with reduced wind loads at $\beta = 90 \pm 15°$ to continue to operate at wind speeds larger than 10 m/s was investigated. Emes *et al.* (2020c) found to achieve an additional 280 MWh of thermal energy collected by heliostat field operation during periods that would conventionally stow the entire field with 24 GWh of annual thermal energy captured. It is therefore apparent that there is a potential to increase the operating performance through consideration of wind load distributions and "smart" stowing strategies of the heliostat field to maximise the energy yield of a power tower plant.

Porous fences were found by Jafari *et al.* (2021) to reduce the turbulence intensity and integral length scales by 20-25% relative to the incoming ABL, but the material cost of perimeter fences for large heliostats and their area of influence into a heliostat field remained a research question. Other methods to reduce the wind loads on heliostats positioned at the inner rows of a field include the attachment of "edge treatment" devices to the heliostat, such as to mitigate the impact of vortex shedding from the leading and trailing edges. Alternatively, the installation of a series of slender plate or rod large-eddy break-up (LEBU) devices at the perimeter of a heliostat field can reduce the effect of the energetic turbulent eddies in the ABL on the heliostat field operation. Characterisation of the flow and wind loads using these methods are required for an improved understanding of their effectiveness. A techno-economic analysis of the cost-effectiveness of fences in heliostat fields is required to assess the sensitivity of reduced loads and heliostat capital cost with respect to the increased land area and material cost of the fence construction.

7. Conclusions

There has been an extensive range of studies on heliostat aerodynamic wind loads in the literature. The aerodynamic coefficients form a basis for the design wind loads on isolated heliostats, which were shown to depend on the geometric parameters of the heliostat, along with wind speed and turbulence parameters in the atmospheric boundary layer (ABL). The following major conclusions can be drawn from the literature to further develop the understanding of the aerodynamic wind loads on heliostats:

1) In wind standards, turbulence intensity and integral length scale profiles are only given for heights above three metres. However, there is demand for smaller heliostats as they are advantageous for high-temperature applications, such as hydrogen production due to lower astigmatism losses. Therefore, field investigations of the wind characteristics between one and three metres height for typical solar sites would be beneficial.
2) The maximum operational loads and the stow survival loads have been defined by the heliostat orientation with respect to the wind. It is most important to model the range of reduced frequencies of the turbulence spectrum that contribute to the unsteady forces on heliostats in wind tunnel experiments in order to reduce the scaling effect on the measured peak wind loads and accurately reproduce the wind loads on the full-scale structure. These maximum heliostat load cases were referenced to design wind speeds and turbulence intensities at a constant height, such as the standard reference height of 10 m in wind load codes and standards. An increased resolution of field-scale wind measurements is essential to understand the effect of surface roughness on the peak aerodynamic coefficients at a range of heliostat field sites to fully characterise the longitudinal and vertical turbulence intensities and length scales that impact the maximum wind loads for operating serviceability and stow survivability considerations.
3) Scaling factors and relationships have been derived in scale-model wind tunnel experiments that account for the variation in wind loads due to geometry effects, such as the aspect ratio, mirror chord length and pylon height from a baseline square-mirror azimuth-elevation heliostat. Further investigations should focus on the influence of wind direction and heliostat

shape due to changes in aspect ratio, and the effect of the gap between the lower heliostat edge and the ground on the aerodynamic coefficients.

4) Dynamic wind loads and modal analysis of local deformations of heliostat components was most effectively investigated in field environments with the mechanical and structural properties of a full-scale heliostat. Due to the large range of heliostat sizes and structural types, the design wind loads are commonly estimated using a combination of peak aerodynamic coefficients and appropriate load-response correlations from finite element models at the relevant design wind speeds. Dynamic amplification factors for alternative heliostat designs to a conventional azimuth-elevation tracking configuration (e.g. spinning axis, tilt-roll) should be further investigated, such as the lowering of the mirror closer to the ground in stow position and resonance effects in the transition to stow due to increases of wind speed at intermediate operating angles.

5) Systematic experimental studies in small-scale boundary layer wind tunnel measurements have effectively simulated the aerodynamics and quasi-static wind loads through investigation of the critical scaling parameters of isolated, tandem and arrays of heliostats over a range of wind turbulence conditions in the ABL. Wind loads on the structural heliostat components, such as bending moment reactions to be resisted by the drives, torque tube and foundation, have been characterised through scale-model testing in wind tunnel experiments. The variation of wind-induced displacements due to operational wind loads on in-field heliostats has been related to the vortex shedding and vibrational modes, but simultaneous load and wake measurements can provide understanding on how the field spacing and orientation affects the operational performance of individual heliostats throughout the field. Instrumenting arrays of heliostats in different rows within a field would also be highly beneficial to better understand the relative contribution of heliostat-generated wake turbulence and incoming ABL turbulence on the heliostat field aerodynamics, wind load distributions and wind-induced tracking errors during operation of a field.

6) It is postulated that the total cost of the heliostat field is conservative as all heliostats are designed based on the maximum wind load coefficients on a single heliostat, while the loads

on heliostats in various rows vary across the field. Heliostat wind loads in arrays have presented wind load reductions on in-field heliostats based on the concept of GBA, however the fence's independent effect was not distinguished from the impact of upstream heliostat blockage. Understanding the variation of wind loads within a heliostat field through the systematic analysis of independent wind load reduction methods can help to improve the field design with respect to the wind loads. Characterisation of the flow and wind loads using favourable methods to reduce heliostat wind loads, such as perimeter and in-field fences and edge treatment devices, should independently assess their cost-effectiveness and feasibility in power tower plants.

There is a strong case for the development of design guidelines for wind load predictions on full-scale heliostats that account for the effects of ABL turbulence based on the scaling of the heliostat structural components and field layout. Such guidelines can benefit the operational performance of the plant and the material costs of manufacturing based on the local wind conditions below heights of 10 metres at different sites. Accurate prediction of the maximum wind loads in real-scale operating conditions provide greater confidence in field efficiency and power tower plant performance models, which enhances the reliability of techno-economic analyses of the solar field operation and structural design of the heliostat components.

Acknowledgements

The authors acknowledge the support from the Australian Solar Thermal Research Institute (ASTRI) and funding provided by the Australian Renewable Energy Agency (ARENA) Grant 1-SRI002.

References

Abengoa Solar (2016), Abengoa, IDC and Khi Community Trust commence commercial operation of Khi Solar One, the first solar tower plant in Africa, https://www.abengoa.com/web/en/noticias_y_publicaciones/noticias/historico/2016/02_febrero/abg_20160205.html, Last Accessed 19 March 2021.

Advisian Worley Group (2021), Khi Solar One 50MW solar power tower plant, https://www.advisian.com/en/case-studies/khi-solar-one-50mw-solar-power-tower-plant, Last Accessed 19 March 2021.

Andraka, C.E., Christian, J.M., Ghanbari, C.M., Gill, D.D., Ho, C.K., Kolb, W.J., Moss, T.A., Smith, E.J. and Yellowhair, J. (2013), "Sandia Capabilities for the Measurement, Characterization, and Analysis of Heliostats for CSP", Sandia National Lab.(SNL-NM), Albuquerque, NM (United States),

Arbes, F., Wöhrbach, M., Gebreiter, D. and Weinrebe, G. (2017) Towards high efficiency heliostat fields. In: Proc., AIP Conference Proceedings,

AS/NZS 1170.2 (2011), "Structural Design Actions - Part 2: Wind actions", Standards Australia and Standards New Zealand, Sydney.

ASCE 7-02 (2002), Minimum design wind loads for buildings and other structures, American Society of Civil Engineers, Reston, Virginia.

ASCE/SEI 7-16 (2016), "Wind loads on building appertenances and other structures: main wind force resisting system (directional procedure)", American Society of Civil Engineers, Reston, Virginia.

Banks, D. (2011) Measuring peak wind loads on solar power assemblies. In: Proc., 13th International Conference on Wind Engineering,

Benammar, S. and Tee, K.F. (2019), Structural reliability analysis of a heliostat under wind load for concentrating solar power, Solar Energy, 181, 43-52.

Blackmon, J.B. (2014), Heliostat drive unit design considerations–Site wind load effects on projected fatigue life and safety factor, Solar energy, 105, 170-180.

Blume, K., Röger, M., Schlichting, T., Macke, A. and Pitz-Paal, R. (2020), Dynamic photogrammetry applied to a real scale heliostat: Insights into the wind-induced behavior and effects on the optical performance, Solar Energy, 212, 297-308.

Bureau of Meteorology (2020), Climate data services, http://www.bom.gov.au/climate/data/, Last Accessed 1 April 2020.

Cook, N.J. (1978), Determination of the model scale factor in wind-tunnel simulations of the adiabatic atmospheric boundary layer, Journal of Wind Engineering and Industrial Aerodynamics, 2(4), 311-321.

Cook, N.J. (1985), “The designer's guide to wind loading of building structures, Part 1: Background, damage survey, wind data and structural classification”, Building Research Establishment, Garston, UK.

Cook, N.J. (1997), The Deaves and Harris ABL model applied to heterogeneous terrain, Journal of Wind Engineering and Industrial Aerodynamics, 66, 197-214.

Counihan, J. (1975), Adiabatic atmospheric boundary layers: a review and analysis of data from the period 1880–1972, Atmospheric Environment, 9(10), 871-905.

De Paepe, W., Pindado, S., Bram, S. and Contino, F. (2016), Simplified elements for wind-tunnel measurements with type-III-terrain atmospheric boundary layer, Measurement, 91, 590-600.

Department of Energy (2017), “The SunShot 2030 Goals”, DOE/EE-1501; Solar Energy Technologies Office, USA.

Durst, C.S. (1960), Wind speeds over short periods of time, Meteorological Magazine, 89(1960), 181-186.

Emes, M., Jafari, A. and Arjomandi, M. (2020b), Wind load design considerations for the elevation and azimuth drives of a heliostat, AIP Conference Proceedings, 2303(1), 030013.

Emes, M., Jafari, A., Collins, M., Wilbert, S., Zarzalejo, L., Siegrist, S. and Arjomandi, M. (2020c) Stowing Strategy for a Heliostat Field Based on Wind Speed and Direction. In: Proc., Proceedings of the 26th SolarPACES 2020 International Conference,

Emes, M.J., Arjomandi, M., Ghanadi, F. and Kelso, R.M. (2017), Effect of turbulence characteristics in the atmospheric surface layer on the peak wind loads on heliostats in stow position, Solar Energy, 157, 284-297.

Emes, M.J., Arjomandi, M., Kelso, R.M. and Ghanadi, F. (2019c), Turbulence length scales in a low-roughness near-neutral atmospheric surface layer, Journal of Turbulence, 20:9, 545-562.

Emes, M.J., Arjomandi, M. and Nathan, G.J. (2015), Effect of heliostat design wind speed on the levelised cost of electricity from concentrating solar thermal power tower plants, Solar Energy, 115, 441-451.

Emes, M.J., Ghanadi, F., Arjomandi, M. and Kelso, R.M. (2018), Investigation of peak wind loads on tandem heliostats in stow position, Renewable Energy, 121, 548-558.

Emes, M.J., Jafari, A., Coventry, J. and Arjomandi, M. (2020a), The influence of atmospheric boundary layer turbulence on the design wind loads and cost of heliostats, Solar Energy, 207, 796-812.

Emes, M.J., Jafari, A., Ghanadi, F. and Arjomandi, M. (2019a), Hinge and overturning moments due to unsteady heliostat pressure distributions in a turbulent atmospheric boundary layer, Solar Energy, 193, 604-617.

Emes, M.J., Jafari, A., Ghanadi, F. and Arjomandi, M. (2019b), A method for the calculation of the design wind loads on heliostats, AIP Conference Proceedings, 2126(1), 030020.

EN 1991-1.4 (2010), Actions on structures, Part 1-4: General actions - Wind actions, Eurocode, Brussels.

ESDU 85020 (2001), Characteristics of atmospheric turbulence near the ground, Part II: single point data for strong winds (neutral atmosphere), Engineering Sciences Data Unit, London.

Farell, C. and Iyengar, A.K. (1999), Experiments on the wind tunnel simulation of atmospheric boundary layers, J Wind Eng Ind Aerodyn, 79(1), 11-35.

Gilooly, S. and Taylor-Power, G. (2016), Physical Modeling of the Atmospheric Boundary Layer in the University of New Hampshire's Flow Physics Facility,

Gong, B., Li, Z., Wang, Z. and Wang, Y. (2012), Wind-induced dynamic response of Heliostat, Renewable Energy, 38(1), 206-213.

Gong, B., Wang, Z., Li, Z., Zang, C. and Wu, Z. (2013), Fluctuating wind pressure characteristics of heliostats, Renewable energy, 50, 307-316.

Griffith, D.T., Moya, A.C., Ho, C.K. and Hunter, P.S. (2012) Structural Dynamics Testing and Analysis for Design Evaluation and Monitoring of Heliostats. In: Proc., ASME 2011 5th International Conference on Energy Sustainability, Griffith, D.T., Moya, A.C., Ho, C.K. and Hunter, P.S. (2015), Structural dynamics testing and analysis for design evaluation and monitoring of heliostats, Journal of Solar Energy Engineering, 137(2), 021010.

Ho, C.K., Griffith, D.T., Sment, J., Moya, A.C., Christian, J.M., Yuan, J.K. and Hunter, P.S. (2012) Dynamic Testing and Analysis of Heliostats to Evaluate Impacts of Wind on Optical Performance and Structural Fatigue. In: Proc., SolarPACES,

Hui, T.M. (2011), Design and optimization of heliostatt field using spinning-elevation sun tracking method based on computational analysis, Master of Engineering, Universiti Tunku Abdul Rahman,

IEC 61400-1 (2005), Wind turbines–part 1: Design requirements, Geneva.

IRENA (2020), “Renewable power generation costs in 2019”, International Renewable Energy Agency, Abu Dhabi.

Iyengar, A.K.S. and Farell, C. (2001), Experimental issues in atmospheric boundary layer simulations: Roughness length and integral length scale determination, Journal of Wind Engineering and Industrial Aerodynamics, 89(11), 1059-1080.

Jafari, A., Emes, M., Cazzolato, B., Ghanadi, F. and Arjomandi, M. (2020a), Turbulence characteristics in the wake of a heliostat in an atmospheric boundary layer flow, Physics of Fluids, 32(4), 045116.

Jafari, A., Emes, M., Cazzolato, B., Ghanadi, F. and Arjomandi, M. (2020b), An experimental investigation of unsteady pressure distribution on tandem heliostats, AIP Conference Proceedings, 2303(1), 030022.

Jafari, A., Emes, M., Cazzolato, B., Ghanadi, F. and Arjomandi, M. (2021), Wire mesh fences for manipulation of turbulence energy spectrum, Experiments in Fluids, 62(2), 30.

Jafari, A., Ghanadi, F., Arjomandi, M., Emes, M.J. and Cazzolato, B.S. (2019a), Correlating turbulence intensity and length scale with the unsteady lift force on flat plates in an atmospheric boundary layer flow, Journal of Wind Eng and Ind Aero, 189, 218-230.

Jafari, A., Ghanadi, F., Emes, M.J., Arjomandi, M. and Cazzolato, B.S. (2018) Effect of Free-stream Turbulence on the Drag Force on a Flat Plate. In: Proc., AFMC, Jafari, A., Ghanadi, F., Emes, M.J., Arjomandi, M. and Cazzolato, B.S. (2019b), Measurement of unsteady wind loads in a wind tunnel: scaling of turbulence spectra, Journal of Wind Eng and Ind Aero, 193, 103955.

Jain, A., Jones, N.P. and Scanlan, R.H. (1996), Coupled flutter and buffeting analysis of long-span bridges, Journal of Structural Engineering, 122(7), 716-725.

Kaimal, J.C. and Finnigan, J.J. (1994), Atmospheric Boundary Layer Flows: Their Structure and Measurement, Oxford University Press.

Kolb, G.J., Ho, C.K., Mancini, T.R. and Gary, J.A. (2011), “Power Tower Technology Roadmap and Cost Reduction Plan”, SAND2011-2419; Sandia National Laboratories, Albuquerque, USA.

Kopp, G.A., Farquhar, S. and Morrison, M.J. (2012), Aerodynamic mechanisms for wind loads on tilted, roof-mounted, solar arrays, Journal of Wind Engineering and Industrial Aerodynamics, 111, 40-52.

Kozmar, H. (2012), Physical modeling of complex airflows developing above rural terrains, Environmental Fluid Mechanics, 12(3), 209-225.

Leitch, C.J., Ginger, J. and Holmes, J. (2016), Wind loads on solar panels mounted parallel to pitched roofs, and acting on the underlying roof, Wind and Structures, 22(3), 307-328.

Li, Q.S., Zhi, L. and Hu, F. (2010), Boundary layer wind structure from observations of a 325 m tower, Journal of Wind Engineering and Industrial Aerodynamics, 98, 818-832.

Mehos, M., Turchi, C., Vidal, J., Wagner, M., Ma, Z., Ho, C., Kolb, W., Andraka, C. and Kruizenga, A. (2017), “Concentrating solar power Gen3 demonstration roadmap”, National Renewable Energy Lab.(NREL), Golden, CO (United States),

Mendis, P., Ngo, T., Haritos, N., Hira, A., Samali, B. and Cheung, J. (2007), Wind loading on tall buildings, EJSE Special Issue: Loading on Structures, 3, 41-54.

Menicucci, A.R., Ho, C.K. and Griffith, D.T. (2012) High Performance Computing for Static and Dynamic Analyses of Heliostats for Concentrating Solar Power. In: Proc., Proceedings of the World Renewable Energy Forum (WREF 2012), Denver, CO, May,

Murphy, L.M. (1980), “Wind loading on tracking and field-mounted solar collectors”, SERI-TP-632-958; Solar Energy Research Institute, Golden, USA.

Nakamura, Y. (1993), Bluff-body aerodynamics and turbulence, J Wind Eng Ind Aerodyn, 49(1), 65-78.

National Climatic Data Center (2020), Climate data online, http://www.ncdc.noaa.gov/cdo-web/datasets, Last Accessed 1 April 2020.

Noone, C.J., Torrilhon, M. and Mitsos, A. (2012), Heliostat field optimization: A new computationally efficient model and biomimetic layout, Solar Energy, 86(2), 792-803.

Peterka, J.A., Bienkiewicz, B., Hosoya, N. and Cermak, J.E. (1987), Heliostat mean wind load reduction, Energy, 12(3-4), 261-267.

Peterka, J.A. and Derickson, R.G. (1992), "Wind load design methods for ground-based heliostats and parabolic dish collectors", SAND92-7009; Sandia National Laboratories, Albuquerque, New Mexico.

Peterka, J.A., Hosoya, N., Bienkiewicz, B. and Cermak, J.E. (1986), "Wind load reduction for heliostats", SERI/STR-253-2859; Colorado State University, Fort Collins, USA.

Peterka, J.A., Hosoya, N., Dodge, S., Cochran, L. and Cermak, J.E. (1998), Area-average peak pressures in a gable roof vortex region, Journal of Wind Engineering and Industrial Aerodynamics, 77-78, 205-215.

Peterka, J.A., Tan, L., Bienkiewcz, B. and Cermak, J.E. (1987), Mean and peak wind load reduction on heliostats, Technical Report for Colorado State University,

Peterka, J.A., Tan, Z., Bienkiewicz, B. and Cermak, J. (1988), "Wind loads on heliostats and parabolic dish collectors: Final subcontractor report", SERI/STR-253-3431; Solar Energy Research Institute, Golden, Colorado.

Peterka, J.A., Tan, Z., Cermak, J.E. and Bienkiewicz, B. (1989), Mean and peak wind loads on heliostats, Journal of Solar Energy Engineering, 111(2), 158-164.

Pfahl, A. (2014a), Survey of heliostat concepts for cost reduction, Journal of Solar Energy Engineering, 136(1),

Pfahl, A. (2018), *Wind loads on heliostats and photovoltaic trackers*, PhD thesis, Technische Universiteit Eindhoven.

Pfahl, A., Brucks, A. and Holze, C. (2014b), Wind load reduction for light-weight heliostats, Energy Procedia, 49, 193-200.

Pfahl, A., Buselmeier, M. and Zaschke, M. (2011a), Wind loads on heliostats and photovoltaic trackers of various aspect ratios, Solar Energy, 85, 2185-2201.

Pfahl, A., Buselmeier, M. and Zaschke, M. (2011c) Determination of wind loads on heliostats. In: Proc., Proceedings of the 17th SolarPACES Conference,

Pfahl, A., Coventry, J., Röger, M., Wolfertstetter, F., Vásquez-Arango, J.F., Gross, F., Arjomandi, M., Schwarzbözl, P., Geiger, M. and Liedke, P. (2017a), Progress in heliostat development, Solar Energy, 152, 3-37.

Pfahl, A., Gross, F., Liedke, P., Hertel, J., Rheinländer, J., Mehta, S., Vásquez-Arango, J.F., Giuliano, S. and Buck, R. (2017b) Reduced to Minimum Cost: Lay-Down Heliostat with Monolithic Mirror-Panel and Closed Loop Control. In: Proc., SolarPACES 2017, Santiago.

Pfahl, A., Randt, M., Holze, C. and Unterschütz, S. (2013), Autonomous light-weight heliostat with rim drives, Solar Energy, 92, 230-240.

Pfahl, A., Randt, M., Meier, F., Zaschke, M., Geurts, C. and Buselmeier, M. (2015), A holistic approach for low cost heliostat fields, Energy Procedia, 69, 178-187.

Pfahl, A. and Uhlemann, P. (2011b), Wind loads on heliostats and photovoltaic trackers at various Reynolds numbers, Journal of Wind Engineering and Industrial Aerodynamics, 99, 964-968.

Price, H., Mehos, M.S., Cable, R., Kearney, D., Kelly, B., Kolb, G. and Morse, F. (2020) CSP plant construction, start-up, and O&M best practices study. In: Proc., AIP Conference Proceedings,

Rasmussen, J.T., Hejlesen, M.M., Larsen, A. and Walther, J.H. (2010), Discrete vortex method simulations of the aerodynamic admittance in bridge aerodynamics, Journal of Wind Engineering and Industrial Aerodynamics, 98(12), 754-766.

Simiu, E. and Scanlan, R.H. (1996), Wind effects on structures: fundamentals and applications to design, John Wiley & Sons.

Sment, J. and Ho, C. (2014), Wind patterns over a heliostat field, Energy Procedia, 49, 229-238.

Stull, R.B. (1988), An introduction to boundary layer meteorology, Kluwer Academic, Dordrecht, Netherlands.

Stull, R.B. (2005), The Atmospheric Boundary Layer, University of British Columbia, Vancouver, Canada.

Sun, H., Gong, B. and Yao, Q. (2014), A review of wind loads on heliostats and trough collectors, Renewable and Sustainable Energy Reviews, 32, 206-221.

Téllez, F., Burisch, M., Villasente, Sánchez, M., Sansom, C., Kirby, P., Turner, P., Caliot, C., Ferriere, A., Bonanos, C.A., Papanicolas, C., Montenon, A., Monterreal, R. and Fernández, J. (2014), "State of the Art in Heliostats and Definition of Specifications", 609837; STAGE-STE Project, Madrid.

Tieleman, H.W. (2003), Wind tunnel simulation of wind loading on low-rise structures: A review, Journal of Wind Engineering and Industrial Aerodynamics, 91(12), 1627-1649.

Turchi, C.S., Boyd, M., Kesseli, D., Kurup, P., Mehos, M.S., Neises, T.W., Sharan, P., Wagner, M.J. and Wendelin, T. (2019), "CSP Systems Analysis-Final Project Report", National Renewable Energy Laboratory (NREL), Golden, Colorado.

Vásquez-Arango, J.F., Buck, R. and Pitz-Paal, R. (2015), Dynamic Properties of a Heliostat Structure Determined by Numerical and Experimental Modal Analysis, Journal of Solar Energy Engineering, 137(5), 051001.

Vasquez Arango, J.F., Pitz-Paal, R. and Breuer, M. (2017), *Dynamic wind loads on heliostats*, PhD Thesis, Lehrstuhl für Solartechnik (DLR).

von Kármán, T. (1948), Progress in the Statistical Theory of Turbulence, Proceedings of the National Academy of Sciences, 34(11), 530-539.

Wolmarans, J.R. and Craig, K. (2019), One-way fluid-structure interaction of a medium-sized heliostat using scale-resolving CFD simulation, Solar Energy, 191, 84-99.

Wu, Z., Gong, B., Wang, Z., Li, Z. and Zang, C. (2010), An experimental and numerical study of the gap effect on wind load on heliostat, Renewable Energy, 35(4), 797-806.

Xiong, Q., Li, Z., Luo, H. and Zhao, Z. (2019), Wind tunnel test study on wind load coefficients variation law of heliostat based on uniform design method, Solar Energy, 184, 209-229.

Xiong, Q., Li, Z., Luo, H., Zhao, Z. and Jiang, A. (2021), Study of probability characteristics and peak value of heliostat support column base shear, Renewable Energy, 168, 1058-1072.

Xu, Y.L. (2013), Wind Effects on Cable-Supported Bridges, John Wiley & Sons, Singapore.

Yu, J.S., Emes, M.J., Ghanadi, F., Arjomandi, M. and Kelso, R.M. (2019), Experimental investigation of peak wind loads on tandem operating heliostats within an atmospheric boundary layer, Solar Energy, 183, 248-259.